Measurement of the $t\bar{t}$ production cross section in $p\bar{p}$ collisions using dilepton events

V.M. Abazov, B. Abbott, M. Abolins, B.S. Acharya, M. Adams, T. Adams, E. Aguilo, S.H. Ahn, M. Ahsan, G.D. Alexeev, et al.

FERMILAB-PUB-07/143-E

Measurement of the $t\bar{t}$ production cross section in $p\bar{p}$ collisions using dilepton events

V.M. Abazov[35], B. Abbott[75], M. Abolins[65], B.S. Acharya[28], M. Adams[51], T. Adams[49], E. Aguilo[5], S.H. Ahn[30], M. Ahsan[59], G.D. Alexeev[35], G. Alkhazov[39], A. Alton[64,*], G. Alverson[63], G.A. Alves[2], M. Anastasoaie[34], L.S. Ancu[34], T. Andeen[53], S. Anderson[45], B. Andrieu[16], M.S. Anzelc[53], Y. Arnoud[13], M. Arov[60], M. Arthaud[17], A. Askew[49], B. Åsman[40], A.C.S. Assis Jesus[3], O. Atramentov[49], C. Autermann[20], C. Avila[7], C. Ay[23], F. Badaud[12], A. Baden[61], L. Bagby[52], B. Baldin[50], D.V. Bandurin[59], S. Banerjee[28], P. Banerjee[28], E. Barberis[63], A.-F. Barfuss[14], P. Bargassa[80], P. Baringer[58], J. Barreto[2], J.F. Bartlett[50], U. Bassler[16], D. Bauer[43], S. Beale[5], A. Bean[58], M. Begalli[3], M. Begel[71], C. Belanger-Champagne[40], L. Bellantoni[50], A. Bellavance[50], J.A. Benitez[65], S.B. Beri[26], G. Bernardi[16], R. Bernhard[22], L. Berntzon[14], I. Bertram[42], M. Besançon[17], R. Beuselinck[43], V.A. Bezzubov[38], P.C. Bhat[50], V. Bhatnagar[26], C. Biscarat[19], G. Blazey[52], F. Blekman[43], S. Blessing[49], D. Bloch[18], K. Bloom[67], A. Boehnlein[50], D. Boline[62], T.A. Bolton[59], G. Borissov[42], K. Bos[33], T. Bose[77], A. Brandt[78], R. Brock[65], G. Brooijmans[70], A. Bross[50], D. Brown[78], N.J. Buchanan[49], D. Buchholz[53], M. Buehler[81], V. Buescher[21], S. Burdin[42,¶], S. Burke[45], T.H. Burnett[82], C.P. Buszello[43], J.M. Butler[62], P. Calfayan[24], S. Calvet[14], J. Cammin[71], S. Caron[33], W. Carvalho[3], B.C.K. Casey[77], N.M. Cason[55], H. Castilla-Valdez[32], S. Chakrabarti[17], D. Chakraborty[52], K.M. Chan[55], K. Chan[5], A. Chandra[48], F. Charles[18], E. Cheu[45], F. Chevallier[13], D.K. Cho[62], S. Choi[31], B. Choudhary[27], L. Christofek[77], T. Christoudias[43], S. Cihangir[50], D. Claes[67], C. Clément[40], B. Clément[18], Y. Coadou[5], M. Cooke[80], W.E. Cooper[50], M. Corcoran[80], F. Couderc[17], M.-C. Cousinou[14], S. Crépé-Renaudin[13], D. Cutts[77], M. Ćwiok[29], H. da Motta[2], A. Das[62], G. Davies[43], K. De[78], S.J. de Jong[34], P. de Jong[33], E. De La Cruz-Burelo[64], C. De Oliveira Martins[3], J.D. Degenhardt[64], F. Déliot[17], M. Demarteau[50], R. Demina[71], D. Denisov[50], S.P. Denisov[38], S. Desai[50], H.T. Diehl[50], M. Diesburg[50], A. Dominguez[67], H. Dong[72], L.V. Dudko[37], L. Duflot[15], S.R. Dugad[28], D. Duggan[49], A. Duperrin[14], J. Dyer[65], A. Dyshkant[52], M. Eads[67], D. Edmunds[65], J. Ellison[48], V.D. Elvira[50], Y. Enari[77], S. Eno[61], P. Ermolov[37], H. Evans[54], A. Evdokimov[73], V.N. Evdokimov[38], A.V. Ferapontov[59], T. Ferbel[71], F. Fiedler[24], F. Filthaut[34], W. Fisher[50], H.E. Fisk[50], M. Ford[44], M. Fortner[52], H. Fox[22], S. Fu[50], S. Fuess[50], T. Gadfort[82], C.F. Galea[34], E. Gallas[50], E. Galyaev[55], C. Garcia[71], A. Garcia-Bellido[82], V. Gavrilov[36], P. Gay[12], W. Geist[18], D. Gelé[18], C.E. Gerber[51], Y. Gershtein[49], D. Gillberg[5], G. Ginther[71], N. Gollub[40], B. Gómez[7], A. Goussiou[55], P.D. Grannis[72], H. Greenlee[50], Z.D. Greenwood[60], E.M. Gregores[4], G. Grenier[19], Ph. Gris[12], J.-F. Grivaz[15], A. Grohsjean[24], S. Grünendahl[50], M.W. Grünewald[29], J. Guo[72], F. Guo[72], P. Gutierrez[75], G. Gutierrez[50], A. Haas[70], N.J. Hadley[61], P. Haefner[24], S. Hagopian[49], J. Haley[68], I. Hall[75], R.E. Hall[47], L. Han[6], K. Hanagaki[50], P. Hansson[40], K. Harder[44], A. Harel[71], R. Harrington[63], J.M. Hauptman[57], R. Hauser[65], J. Hays[43], T. Hebbeker[20], D. Hedin[52], J.G. Hegeman[33], J.M. Heinmiller[51], A.P. Heinson[48], U. Heintz[62], C. Hensel[58], K. Herner[72], G. Hesketh[63], M.D. Hildreth[55], R. Hirosky[81], J.D. Hobbs[72], B. Hoeneisen[11], H. Hoeth[25], M. Hohlfeld[21], S.J. Hong[30], R. Hooper[77], S. Hossain[75], P. Houben[33], Y. Hu[72], Z. Hubacek[9], V. Hynek[8], I. Iashvili[69], R. Illingworth[50], A.S. Ito[50], S. Jabeen[62], M. Jaffré[15], S. Jain[75], K. Jakobs[22], C. Jarvis[61], R. Jesik[43], K. Johns[45], C. Johnson[70], M. Johnson[50], A. Jonckheere[50], P. Jonsson[43], A. Juste[50], D. Käfer[20], S. Kahn[73], E. Kajfasz[14], A.M. Kalinin[35], J.R. Kalk[65], J.M. Kalk[60], S. Kappler[20], D. Karmanov[37], J. Kasper[62], P. Kasper[50], I. Katsanos[70], D. Kau[49], R. Kaur[26], V. Kaushik[78], R. Kehoe[79], S. Kermiche[14], N. Khalatyan[38], A. Khanov[76], A. Kharchilava[69], Y.M. Kharzheev[35], D. Khatidze[70], H. Kim[31], T.J. Kim[30], M.H. Kirby[34], M. Kirsch[20], B. Klima[50], J.M. Kohli[26], J.-P. Konrath[22], M. Kopal[75], V.M. Korablev[38], B. Kothari[70], A.V. Kozelov[38], D. Krop[54], A. Kryemadhi[81], T. Kuhl[23], A. Kumar[69], S. Kunori[61], A. Kupco[10], T. Kurča[19], J. Kvita[8], F. Lacroix[12], D. Lam[55], S. Lammers[70], G. Landsberg[77], J. Lazoflores[49], P. Lebrun[19], W.M. Lee[50], A. Leflat[37], F. Lehner[41], J. Lellouch[16], V. Lesne[12], J. Leveque[45], P. Lewis[43], J. Li[78], Q.Z. Li[50], L. Li[48], S.M. Lietti[4], J.G.R. Lima[52], D. Lincoln[50], J. Linnemann[65], V.V. Lipaev[38], R. Lipton[50], Y. Liu[6], Z. Liu[5], L. Lobo[43], A. Lobodenko[39], M. Lokajicek[10], A. Lounis[18], P. Love[42], H.J. Lubatti[82], A.L. Lyon[50], A.K.A. Maciel[2], D. Mackin[80], R.J. Madaras[46], P. Mättig[25], C. Magass[20], A. Magerkurth[64], N. Makovec[15], P.K. Mal[55], H.B. Malbouisson[3], S. Malik[67], V.L. Malyshev[35], H.S. Mao[50], Y. Maravin[59], B. Martin[13], R. McCarthy[72], A. Melnitchouk[66], A. Mendes[14], L. Mendoza[7], P.G. Mercadante[4], M. Merkin[37], K.W. Merritt[50], J. Meyer[21], A. Meyer[20], M. Michaut[17], T. Millet[19], J. Mitrevski[70], J. Molina[3], R.K. Mommsen[44], N.K. Mondal[28], R.W. Moore[5], T. Moulik[58], G.S. Muanza[19], M. Mulders[50], M. Mulhearn[70], O. Mundal[21], L. Mundim[3], E. Nagy[14], M. Naimuddin[50], M. Narain[77], N.A. Naumann[34], H.A. Neal[64], J.P. Negret[7], P. Neustroev[39], H. Nilsen[22], A. Nomerotski[50], S.F. Novaes[4], T. Nunnemann[24], V. O'Dell[50], D.C. O'Neil[5], G. Obrant[39], C. Ochando[15], D. Onoprienko[59], N. Oshima[50], J. Osta[55], R. Otec[9], G.J. Otero y Garzón[51], M. Owen[44], P. Padley[80], M. Pangilinan[77],

N. Parashar[56], S.-J. Park[71], S.K. Park[30], J. Parsons[70], R. Partridge[77], N. Parua[54], A. Patwa[73], G. Pawloski[80], B. Penning[22], P.M. Perea[48], K. Peters[44], Y. Peters[25], P. Pétroff[15], M. Petteni[43], R. Piegaia[1], J. Piper[65], M.-A. Pleier[21], P.L.M. Podesta-Lerma[32,§], V.M. Podstavkov[50], Y. Pogorelov[55], M.-E. Pol[2], P. Polozov[36], A. Pompoˇ, B.G. Pope[65], A.V. Popov[38], C. Potter[5], W.L. Prado da Silva[3], H.B. Prosper[49], S. Protopopescu[73], J. Qian[64], A. Quadt[21], B. Quinn[66], A. Rakitine[42], M.S. Rangel[2], K.J. Rani[28], K. Ranjan[27], P.N. Ratoff[42], P. Renkel[79], S. Reucroft[63], P. Rich[44], M. Rijssenbeek[72], I. Ripp-Baudot[18], F. Rizatdinova[76], S. Robinson[43], R.F. Rodrigues[3], C. Royon[17], P. Rubinov[50], R. Ruchti[55], G. Safronov[36], G. Sajot[13], A. Sánchez-Hernández[32], M.P. Sanders[16], A. Santoro[3], G. Savage[50], L. Sawyer[60], T. Scanlon[43], D. Schaile[24], R.D. Schamberger[72], Y. Scheglov[39], H. Schellman[53], P. Schieferdecker[24], T. Schliephake[25], C. Schmitt[25], C. Schwanenberger[44], A. Schwartzman[68], R. Schwienhorst[65], J. Sekaric[49], S. Sengupta[49], H. Severini[75], E. Shabalina[51], M. Shamim[59], V. Shary[17], A.A. Shchukin[38], R.K. Shivpuri[27], D. Shpakov[50], V. Siccardi[18], V. Simak[9], V. Sirotenko[50], P. Skubic[75], P. Slattery[71], D. Smirnov[55], R.P. Smith[50], J. Snow[74], G.R. Snow[67], S. Snyder[73], S. Söldner-Rembold[44], L. Sonnenschein[16], A. Sopczak[42], M. Sosebee[78], K. Soustruznik[8], M. Souza[2], B. Spurlock[78], J. Stark[13], J. Steele[60], V. Stolin[36], A. Stone[51], D.A. Stoyanova[38], J. Strandberg[64], S. Strandberg[40], M.A. Strang[69], M. Strauss[75], E. Strauss[72], R. Ströhmer[24], D. Strom[53], M. Strovink[46], L. Stutte[50], S. Sumowidagdo[49], P. Svoisky[55], A. Sznajder[3], M. Talby[14], P. Tamburello[45], A. Tanasijczuk[1], W. Taylor[5], P. Telford[44], J. Temple[45], B. Tiller[24], F. Tissandier[12], M. Titov[17], V.V. Tokmenin[35], M. Tomoto[50], T. Toole[61], I. Torchiani[22], T. Trefzger[23], D. Tsybychev[72], B. Tuchming[17], C. Tully[68], P.M. Tuts[70], R. Unalan[65], S. Uvarov[39], L. Uvarov[39], S. Uzunyan[52], B. Vachon[5], P.J. van den Berg[33], B. van Eijk[33], R. Van Kooten[54], W.M. van Leeuwen[33], N. Varelas[51], E.W. Varnes[45], A. Vartapetian[78], I.A. Vasilyev[38], M. Vaupel[25], P. Verdier[19], L.S. Vertogradov[35], M. Verzocchi[50], F. Villeneuve-Seguier[43], P. Vint[43], J.-R. Vlimant[16], P. Vokac[9], E. Von Toerne[59], M. Voutilainen[67,‡], M. Vreeswijk[33], R. Wagner[68], H.D. Wahl[49], L. Wang[61], M.H.L.S Wang[50], J. Warchol[55], G. Watts[82], M. Wayne[55], M. Weber[50], G. Weber[23], H. Weerts[65], A. Wenger[22,#], N. Wermes[21], M. Wetstein[61], A. White[78], D. Wicke[25], G.W. Wilson[58], S.J. Wimpenny[48], M. Wobisch[60], D.R. Wood[63], T.R. Wyatt[44], Y. Xie[77], S. Yacoob[53], R. Yamada[50], M. Yan[61], T. Yasuda[50], Y.A. Yatsunenko[35], K. Yip[73], H.D. Yoo[77], S.W. Youn[53], J. Yu[78], C. Yu[13], A. Yurkewicz[72], A. Zatserklyaniy[52], C. Zeitnitz[25], D. Zhang[50], T. Zhao[82], B. Zhou[64], J. Zhu[72], M. Zielinski[71], D. Zieminska[54], A. Zieminski[54], L. Zivkovic[70], V. Zutshi[52], and E.G. Zverev[37]

(The DØ Collaboration)

[1]*Universidad de Buenos Aires, Buenos Aires, Argentina*
[2]*LAFEX, Centro Brasileiro de Pesquisas Físicas, Rio de Janeiro, Brazil*
[3]*Universidade do Estado do Rio de Janeiro, Rio de Janeiro, Brazil*
[4]*Instituto de Física Teórica, Universidade Estadual Paulista, São Paulo, Brazil*
[5]*University of Alberta, Edmonton, Alberta, Canada, Simon Fraser University, Burnaby, British Columbia, Canada, York University, Toronto, Ontario, Canada, and McGill University, Montreal, Quebec, Canada*
[6]*University of Science and Technology of China, Hefei, People's Republic of China*
[7]*Universidad de los Andes, Bogotá, Colombia*
[8]*Center for Particle Physics, Charles University, Prague, Czech Republic*
[9]*Czech Technical University, Prague, Czech Republic*
[10]*Center for Particle Physics, Institute of Physics, Academy of Sciences of the Czech Republic, Prague, Czech Republic*
[11]*Universidad San Francisco de Quito, Quito, Ecuador*
[12]*Laboratoire de Physique Corpusculaire, IN2P3-CNRS, Université Blaise Pascal, Clermont-Ferrand, France*
[13]*Laboratoire de Physique Subatomique et de Cosmologie, IN2P3-CNRS, Universite de Grenoble 1, Grenoble, France*
[14]*CPPM, IN2P3-CNRS, Université de la Méditerranée, Marseille, France*
[15]*Laboratoire de l'Accélérateur Linéaire, IN2P3-CNRS et Université Paris-Sud, Orsay, France*
[16]*LPNHE, IN2P3-CNRS, Universités Paris VI and VII, Paris, France*
[17]*DAPNIA/Service de Physique des Particules, CEA, Saclay, France*
[18]*IPHC, Université Louis Pasteur et Université de Haute Alsace, CNRS, IN2P3, Strasbourg, France*
[19]*IPNL, Université Lyon 1, CNRS/IN2P3, Villeurbanne, France and Université de Lyon, Lyon, France*
[20]*III. Physikalisches Institut A, RWTH Aachen, Aachen, Germany*
[21]*Physikalisches Institut, Universität Bonn, Bonn, Germany*
[22]*Physikalisches Institut, Universität Freiburg, Freiburg, Germany*
[23]*Institut für Physik, Universität Mainz, Mainz, Germany*

[24]*Ludwig-Maximilians-Universität München, München, Germany*
[25]*Fachbereich Physik, University of Wuppertal, Wuppertal, Germany*
[26]*Panjab University, Chandigarh, India*
[27]*Delhi University, Delhi, India*
[28]*Tata Institute of Fundamental Research, Mumbai, India*
[29]*University College Dublin, Dublin, Ireland*
[30]*Korea Detector Laboratory, Korea University, Seoul, Korea*
[31]*SungKyunKwan University, Suwon, Korea*
[32]*CINVESTAV, Mexico City, Mexico*
[33]*FOM-Institute NIKHEF and University of Amsterdam/NIKHEF, Amsterdam, The Netherlands*
[34]*Radboud University Nijmegen/NIKHEF, Nijmegen, The Netherlands*
[35]*Joint Institute for Nuclear Research, Dubna, Russia*
[36]*Institute for Theoretical and Experimental Physics, Moscow, Russia*
[37]*Moscow State University, Moscow, Russia*
[38]*Institute for High Energy Physics, Protvino, Russia*
[39]*Petersburg Nuclear Physics Institute, St. Petersburg, Russia*
[40]*Lund University, Lund, Sweden, Royal Institute of Technology and Stockholm University, Stockholm, Sweden, and Uppsala University, Uppsala, Sweden*
[41]*Physik Institut der Universität Zürich, Zürich, Switzerland*
[42]*Lancaster University, Lancaster, United Kingdom*
[43]*Imperial College, London, United Kingdom*
[44]*University of Manchester, Manchester, United Kingdom*
[45]*University of Arizona, Tucson, Arizona 85721, USA*
[46]*Lawrence Berkeley National Laboratory and University of California, Berkeley, California 94720, USA*
[47]*California State University, Fresno, California 93740, USA*
[48]*University of California, Riverside, California 92521, USA*
[49]*Florida State University, Tallahassee, Florida 32306, USA*
[50]*Fermi National Accelerator Laboratory, Batavia, Illinois 60510, USA*
[51]*University of Illinois at Chicago, Chicago, Illinois 60607, USA*
[52]*Northern Illinois University, DeKalb, Illinois 60115, USA*
[53]*Northwestern University, Evanston, Illinois 60208, USA*
[54]*Indiana University, Bloomington, Indiana 47405, USA*
[55]*University of Notre Dame, Notre Dame, Indiana 46556, USA*
[56]*Purdue University Calumet, Hammond, Indiana 46323, USA*
[57]*Iowa State University, Ames, Iowa 50011, USA*
[58]*University of Kansas, Lawrence, Kansas 66045, USA*
[59]*Kansas State University, Manhattan, Kansas 66506, USA*
[60]*Louisiana Tech University, Ruston, Louisiana 71272, USA*
[61]*University of Maryland, College Park, Maryland 20742, USA*
[62]*Boston University, Boston, Massachusetts 02215, USA*
[63]*Northeastern University, Boston, Massachusetts 02115, USA*
[64]*University of Michigan, Ann Arbor, Michigan 48109, USA*
[65]*Michigan State University, East Lansing, Michigan 48824, USA*
[66]*University of Mississippi, University, Mississippi 38677, USA*
[67]*University of Nebraska, Lincoln, Nebraska 68588, USA*
[68]*Princeton University, Princeton, New Jersey 08544, USA*
[69]*State University of New York, Buffalo, New York 14260, USA*
[70]*Columbia University, New York, New York 10027, USA*
[71]*University of Rochester, Rochester, New York 14627, USA*
[72]*State University of New York, Stony Brook, New York 11794, USA*
[73]*Brookhaven National Laboratory, Upton, New York 11973, USA*
[74]*Langston University, Langston, Oklahoma 73050, USA*
[75]*University of Oklahoma, Norman, Oklahoma 73019, USA*
[76]*Oklahoma State University, Stillwater, Oklahoma 74078, USA*
[77]*Brown University, Providence, Rhode Island 02912, USA*
[78]*University of Texas, Arlington, Texas 76019, USA*
[79]*Southern Methodist University, Dallas, Texas 75275, USA*
[80]*Rice University, Houston, Texas 77005, USA*
[81]*University of Virginia, Charlottesville, Virginia 22901, USA and*
[82]*University of Washington, Seattle, Washington 98195, USA*

(Dated: June 4, 2007)

We present a measurement of the $t\bar{t}$ pair production cross section in $p\bar{p}$ collisions at $\sqrt{s} = 1.96$ TeV utilizing approximately 425 pb^{-1} of data collected with the D0 detector. We consider decay channels containing two high p_T charged leptons (either e or μ) from leptonic decays of both top-daughter W bosons. These were gathered using four sets of selection criteria, three of which required that a pair of fully identified leptons (*i.e.*, $e\mu$, ee, or $\mu\mu$) be found. The fourth approach imposed less restrictive criteria on one of the lepton candidates and required that at least one hadronic jet in each event be tagged as containing a b quark. For a top quark mass of 175 GeV, the measured cross section is 7.4 ±1.4 (stat) ±1.0 (syst) pb and for the current Tevatron average top quark mass of 170.9 GeV, the resulting value of the cross section is 7.8 ±1.8 (stat+syst) pb.

PACS numbers: 13.85.Lg, 13.85.Qk, 14.65.Ha

I. INTRODUCTION

A. The Top Quark

The top quark, first observed by the CDF and D0 collaborations in 1995 [1, 2], is the heaviest elementary particle so far observed. Its mass is sufficient to allow decay to hypothesized particles such as the charged Higgs and to probe electroweak symmetry breaking physics. At the Fermilab Tevatron Collider, top quark production occurs predominantly in top-antitop quark ($t\bar{t}$) pairs. For a center of mass energy of $\sqrt{s} = 1.96$ TeV, leading order QCD suggests that $t\bar{t}$ production results from quark-antiquark annihilation about 85% of the time, while gluon-gluon fusion is responsible for the remaining 15% [3]. Recent theoretical calculations predict, for an assumed top quark mass (m_t) of 175 GeV, an inclusive top quark pair production cross section at $\sqrt{s} = 1.96$ TeV of 6.7 pb with an uncertainty of less than 15% [4, 5]. If the observed production cross section were to differ significantly from the standard model prediction, it would be evidence of new physics, such as exotic top quark decays or new production mechanisms such as $t\bar{t}$ resonances [6]. Significant deviation among measured cross sections obtained from the observations of different top quark decay channels would also indicate the presence of new physics. It is therefore important to precisely measure the top quark pair production cross section using each possible final state. Previous measurements by the CDF and D0 experiments [3, 7, 8, 9] show good agreement with the theoretical expectation within uncertainties. The most precise cross section measurement reported by D0 is 6.6±1.0 pb [9] in the lepton+jets final state and using secondary vertex tagging algorithm to identify b jets.

B. Top Quark Decays and the Dilepton Signature

According to the standard model, the top quark decays almost 100% of the time to a W boson and a b quark. For approximately 6% of $t\bar{t}$ pairs, both W bosons decay leptonically to generate a final state containing a pair of electrons, a pair of muons, or an electron and a muon [3]. This produces a unique event signature consisting of two high transverse momentum (p_T) charged leptons, significant missing transverse energy ($\not\!\!E_T$) from the associated neutrinos, and two high p_T jets from the b quarks.

Despite low branching ratios relative to channels with hadronic W boson decays, the dilepton channels are advantageous for study because few standard model background processes have two high p_T leptons and neutrinos in their final states. Those which do usually do not contain two high p_T jets. For example, electroweak diboson production can result in two isolated, high p_T leptons and neutrinos, but suffers from a low cross section and can be discriminated against by requiring high p_T jets. Drell-Yan production of (Z/γ^*)+jets events has no direct decay process to dilepton final states with real neutrinos. (Z/γ^*) decay to τ particles produces neutrinos but suffers from a low branching ratio and a softer lepton p_T spectrum relative to top quark events.

C. The Content of this Article

This paper describes a new measurement of top quark decays to final states containing a pair of electrons or muons, or one electron and one muon. Section II contains a description of the experimental setup used to collect the data used for the measurement. A discussion of the Monte Carlo samples that aided our interpretation of this data is in Sec. III. Section IV includes a description of the triggering system used to acquire the data, and Sec. V contains descriptions of the offline reconstruction techniques used to compute the physical quantities critical to the extraction of the top quark signal. Discussion of the methods used to identify each dilepton decay mode in the data sample is in Sec. VI. Finally, the computation of the top quark pair production cross section is described in Sec. VII and the result is summarized in Sec. VIII.

II. EXPERIMENTAL APPARATUS

A. The Fermilab Tevatron Collider's Run II

The Fermilab Tevatron Collider, a proton anti-proton accelerator, collided beams at a center-of-mass energy of 1.8 TeV during the period of operation (Run I) between 1992 and 1996. The D0 detector, one of two multipurpose detectors designed to study the high energy collisions at Fermilab, collected approximately 120 pb^{-1} of data during Run I [10]. After significant improvements to both the accelerator and the D0 detector, Run II began in March 2001 with the collider operating at a center-of-mass energy of 1.96 TeV. The increased energy brought an increase in the top quark pair production cross section of ≈30%. The analyses discussed in this paper are based on approximately 425 pb^{-1} of data collected by D0 between April 2002 and August 2004. D0 has performed a similar measurement using ∼230 pb^{-1} of data [8].

B. The D0 Detector

This section presents an overview of the experimental apparatus, emphasizing the subsystems most relevant to the $t\bar{t}$ production cross section measurement. A more complete description of the upgraded experiment can be found in Ref. [11].

The D0 detector comprises three major subsystems which together identify and measure the energy or momentum of electrons, jets, muons, and (indirectly) neutrinos — all of which can be found in the final states of $t\bar{t}$ decays. The subsystems are the central tracking detectors, a uranium/liquid-argon calorimeter, and a muon spectrometer.

The spatial coordinates of the D0 detector are defined as follows: the positive z direction is along the direction of the proton motion while positive y is defined as upward with respect to the detector's center, which serves as the origin. The polar angle θ is measured with respect to the positive z direction and the azimuthal angle ϕ is measured with respect to the positive x direction. The radial distance r is the perpendicular displacement from the z axis. The polar direction is more usually described by the pseudorapidity, defined as $\eta \equiv -\ln(\tan\theta/2)$.

The central tracking detectors consist of a silicon microstrip tracker (SMT) and a central scintillating fiber tracker (CFT) located within a 2 T solenoidal magnetic field. Together these detectors are responsible for locating the position of the hard scatter and for measuring the trajectories and momenta of charged particles. The SMT can also locate displaced, secondary vertices which aid in heavy quark tagging. It is composed of high-resistivity silicon sensors arranged in barrels and disks to maximize the detector surface area perpendicular to charged particle trajectories. The barrel detectors provide tracking information at central values of $|\eta|$ (< 1.5), while the disks extend coverage out to $|\eta| \approx 3.0$. The CFT is constructed from scintillating fibers mounted on eight concentric support cylinders. Each cylinder supports an axial layer of fibers oriented along z and a stereo layer oriented at a slight angle with respect to z. The outermost cylinder provides coverage for $|\eta| < 1.7$.

The liquid-argon calorimeter surrounds the central tracking detectors. In addition to providing energy measurements for electrons, photons, and jets, it can distinguish showers generated by electrons or photons from those produced by hadrons. The calorimeter also plays a critical role in the measurement of the event-wide transverse energy balance used to identify neutrinos. The system is composed of three parts: a central calorimeter (CC) which provides coverage to $|\eta| \approx 1$ and north and south endcap calorimeters (EC) which extend coverage to $|\eta| \approx 4$. Because each calorimeter is housed in its own cryostat, there is a gap in coverage between each EC and the CC, the region defined by $1.0 < |\eta| < 1.4$. To partially compensate for this, an intercryostat detector (ICD) made of a series of scintillating tiles is located between the CC and EC cryostats.

Each calorimeter section has three subsections: an inner electromagnetic (EM) section which uses thin uranium absorber plates, a fine hadronic section which uses uranium-niobium alloy plates, and a coarse hadronic section which uses copper or stainless steel absorber plates in the CC or EC, respectively. The calorimeters are transversely divided into *projective* towers, so-called because the rays along which the calorimeter cells are oriented project outward from the interaction center. Each tower layer is further divided into segments of size $\Delta\eta \times \Delta\phi = 0.1 \times 2\pi/64$, except for the third layer of the EM section which is segmented twice as finely to allow for more precise measurement of the EM shower centroid.

The muon spectrometer surrounds the calorimeter cryostats and uses a combination of wire chambers and scintillation counters to obtain precise muon spatial and timing information, respectively. Like the calorimeter, the muon spectrometer consists of three separate subdetectors. The central detector covers approximately $|\eta| < 1.0$ and the forward systems extend to $|\eta| \approx 2$. Each system contains three layers of instrumentation, and a 1.8 T iron toroidal magnet is located between the innermost and second layers. Each layer contains both wire chambers and scintillation counters. The scintillators have response times sufficiently fast to allow for both muon triggering and out-of-time background rejection.

The wire chambers in the central region are proportional drift tubes (PDTs) oriented to provide maximum resolution for measuring muon bending angles produced by the toroidal magnetic field. The innermost central scintillation counters are segmented in 4.5° increments in ϕ to match the CFT segmentation. Each layer of the forward spectrometers contains several strata of mini drift tubes (MDTs) and a set of scintillation counters referred to as *pixels*. The pixels are projectively arranged from the interaction point with a ϕ segmentation of 4.5° and an η segmentation of ≈0.12.

The luminosity measurement is based on the rate of inelastic $p\bar{p}$ collisions observed by the luminosity monitors (LM) mounted in front of the EC cryostats at $z = \pm 140$ cm. The LM consists of two arrays of 24 plastic scintillator counters with photomultiplier readout, and covers the $|\eta|$ range between 2.7 and 4.4. The uncertainty on the luminosity measurement is currently estimated to be ± 6.1% [12].

III. EVENT SIMULATION

Selection efficiencies for $t\bar{t}$ signal events and background survival rates for each of the analyses were computed using Monte Carlo simulations of each of the physics processes contributing to the observed event yields. This section provides some details regarding the generation of the Monte Carlo samples used.

Simulation began with initial parton generation. In general, this was achieved using the ALPGEN [13] generator, which contains the exact leading-order (LO) matrix elements for the processes discussed in the following sections. Unless otherwise specified, output from ALPGEN was then convoluted with the CTEQ5L [14] parton distribution functions (PDFs). Parton showering was carried out using PYTHIA [15]. Decays of B mesons were simulated with EVTGEN [16] and τ-lepton decays were simulated with TAUOLA [17].

After the modeling of quark and gluon hadronization and unstable particle decays, the list of generated objects was passed through a GEANT-based [18] model of the D0 detector. This provides a detailed simulation of the effects of detector composition and geometry. Resolutions for momenta and energies of leptons and jets, as well as efficiencies for their identification, were determined in data and compared to their counterparts in Monte Carlo. Observed discrepancies were used to correct the simulated samples.

A. $\mathbf{t\bar{t}}$ Production

Detector acceptance, object reconstruction efficiencies, and the effects of kinematical cuts were estimated with a sample of simulated $t\bar{t} \to \ell\ell + X$ decays, where $\ell = e$, μ, or τ. Seven samples were generated with the following values of top quark mass (m_t): 140, 160, 175, 190, and 210 GeV. These were used to parameterize the signal acceptances as functions of m_t. The central value of the cross section was computed for $m_t = 175$ GeV.

B. $(\mathbf{Z}/\gamma^*)$+jets Processes

The largest background to the $t\bar{t}$ dilepton signal arises from Drell-Yan Z/γ^* production and leptonic decay with associated production of one or more jets. To aid in the estimation of these backgrounds, we generated $Z/\gamma^* \to \ell\ell$ events with one or two partons. For each lepton flavor we generated three $M_{\ell\ell}$ regions: 15–60 GeV, 60–130 GeV, and >130 GeV. The relative weights of the three samples were determined from the ratios of their LO cross sections.

The absolute normalizations of these background samples were set by the number of Z/γ^*+jets $\to \ell\ell$+jets events observed in control samples selected from data. These were chosen by requiring that the reconstructed dilepton mass be near the Z boson mass so that the samples were rejected by the signal selection criteria described in Secs. VI C and VI D. This normalization was carried out at an early stage of event selection where the $t\bar{t}$ yield is a negligible fraction of the selected sample. The efficiency of further kinematical selections for Z/γ^* events was then derived from the details of the simulated samples.

C. Diboson+jets Production

$WW \to \ell\ell + X$ and $WZ \to \ell\ell + X$ (where $\ell = e$ or μ) production in association with one or two jets contributes to a lesser degree to the selected samples. As for all the other Monte Carlo samples used, we generated these processes at LO with ALPGEN, but the impact of PDFs was simulated using CTEQ4L [19]. The resulting samples were normalized using the ratio of NLO to LO diboson production cross sections calculated without explicit jet requirements. [20].

IV. TRIGGERING

The analyses described in this paper made use of data collected by triggering on the presence of objects consistent with the dilepton signature: electrons, muons, central tracks, and jets. Correlations between these objects and event-wide variables like $\not\!\!E_T$, though available at all trigger levels, were not utilized in data collection. This section begin with a brief description of the D0 trigger system and then provides a description of the triggering conditions used to collect the dilepton samples analyzed. A more detailed discussion of the triggering system is available in Ref. [11].

A. The D0 Triggering System

The D0 triggering system consists of three separate levels, each of which examines successively fewer events in ever greater detail. The first stage (Level 1) is a collection of custom hardware triggers that accepts data from all the major detector subsystems at a rate of 1.7 MHz and generates an acceptance rate of around or below 2 kHz. In the second stage (Level 2), microprocessors associated with each detector subsystem reconstruct physics objects which are passed on to a global processor that generates decisions based upon all the objects in an event. Level 2 provides a maximum accept rate of around 1 kHz. The final trigger stage (Level 3), applies more sophisticated algorithms to data from precision readout of the detector components to further reduce the overall acceptance rate to around 50 Hz. Events passing Level 3 are written to tape.

At Level 1, the muon trigger searches for patterns of scintillator and wire chamber hits consistent with muons traversing the multiple layers of the muon detector. *Loose* Level 1 muons are constructed from scintillator hits only, while *tight* muons include corresponding patterns of hits in wire chambers [29]. Additionally, some Level 1 muon triggers require that a matching track be found by the central track trigger (CTT). CTT tracks are found by analyzing patterns of axial CFT hits. All eight axial layers must register a hit, and the curvature of the resulting patterns provides a p_T estimate that is used for a threshold requirement.

At Level 2, the muon-finding algorithm uses more precise timing information to improve the quality of muon candidates. In general, a combination of wire and scintillator hits both inside and outside the toroid iron is required. Level 3 uses tracks found in the central tracker to identify the most probable position for the hard scatter. This position, also called the primary vertex, is used to refine momentum estimates from reconstructed muon-track bending by the toroidal field, and the result is used to apply momentum threshold requirements. Additionally, Level 3 is capable of reconstructing central tracks with hits missing and its algorithms make use of CFT stereo information.

The Level 1 calorimeter trigger inputs are electromagnetic (EM) and hadronic (H) trigger tower energies summed over a transverse area of $\Delta\eta \times \Delta\phi = 0.2 \times 0.2$. Electron candidates only include energy collected in the EM section of the calorimeter, while jet candidate energies include the H towers. At Level 2, calorimeter objects are reconstructed from trigger towers using the Level 1 objects as seeds. The Level 2 jet algorithm clusters 5 $\times$ 5 groups of towers centered on the seed towers. Electron candidates are formed by clustering each EM seed with the highest E_T neighboring tower.

The Level 3 calorimeter triggers use the precision readout chain and the reconstructed primary vertex position to improve energy and position resolution relative to Level 2. Jets and electrons are formed using a simple cone algorithm [21]. *Loose* Level 3 electrons must have most of their energy deposited in the EM layers and they must meet basic shower shape criteria. *Tight* Level 3 electrons must survive additional shape criteria. Additional background suppression is also achieved in some triggers by requiring that a matching central track be found.

B. Dilepton Triggers

The triggers used to collect the dilepton samples required that the lepton signatures distinguishing each channel were present at multiple triggering levels. In order to reduce rate but maintain overall trigger efficiency for a given channel, a logical OR of multiple triggers having different conditions tightened in a complementary manner was sometimes used. Brief summaries of the trigger conditions used for each analysis channel are presented here, and more detailed breakdowns of the requirements are available in Appendix A.

The $e\mu$ triggers required that an electron with an E_T of at least 5 GeV and a loose muon were found at Level 1. In some cases a Level 2 muon was also required, but otherwise the remaining conditions involved electrons reconstructed at Level 3. A loose Level 3 electron with $E_T > 10$ GeV was always included in the requirements, and at higher luminosity the energy threshold was increased and this requirement was combined in an OR with a tight electron with $E_T > 5$ GeV.

The dielectron triggers usually included the requirement that two electrons, each with $E_T > 6$ GeV, were found at Level 1. In some cases only one electron with $E_T > 11$ GeV was required at Level 1. A Level 2 requirement was only included for later periods containing high luminosity conditions. It required that two electrons, each with $E_T > 18$ GeV, be found. The Level 3 condition always included at least one loose electron with $E_T > 10$ GeV. For later data taking periods, a second electron was added to the Level 3 condition, and the energy threshold and quality requirements were tightened.

To maximize efficiency, the $\mu\mu$ channel made use of high p_T single muon triggers and switched to dimuon trigger requirements when the single muon triggers were prescaled due to high rates. The single muon triggers required a tight muon at Level 1, while the dimuon triggers used loose Level 1 muons. All triggers used for the dimuon channel demanded that one muon be found at Level 2, sometimes with a $p_T > 3$ GeV requirement. The Level 3 requirements also involved single muon signatures, but complementary conditions were sometimes combined in a logical OR. These signatures included a Level 3 muon with a p_T of at least 6 GeV or a Level 3 central track with a p_T of at least 5 GeV.

Since the ℓ+track channels did not require that two identified leptons be found in each candidate event, they relied on high p_T single lepton triggers. In some cases these triggers included jet requirements. At Level 1, the e+track triggers demanded the presence of either one EM object with $E_T > 10$ GeV or two EM objects, each with $E_T > 3$ GeV. In some cases the single electron condition was coupled with the requirement that two Level 1 jets were found, each with $E_T > 5$ GeV. The Level 2 conditions included the presence of one electron with $E_T > 10$ GeV. Some triggers also asked that two jets, each with $E_T > 10$ GeV, be found at Level 2. Level 3 requirements included at least one electron with $E_T > 15$ GeV. Some triggers also required that two jets, each with $E_T > 15$ GeV, be found at Level 3.

The μ+track triggers required that at least one loose Level 1 muon, sometimes with a matching central track, be found. Some triggers also demanded that at least one jet with $E_T > 3$ GeV be found. The Level 2 conditions usually required that one muon be found and sometimes also required one jet with $E_T > 8$ GeV to be present. Level 3 conditions alternately included 1 jet with $E_T > 10$ GeV, one muon with $p_T > 15$ GeV, or one central track with $p_T > 10$ GeV. Sometimes the track and muon requirements were combined in a logical OR.

The efficiencies of trigger conditions on single objects were estimated using data samples selected to remove triggering bias. The efficiency for a $t\bar{t}$ event to satisfy a trigger condition was then estimated by folding per-muon, per-electron, and per-jet efficiencies into Monte

Carlo simulated events. A similar process was used for those background estimations that are based upon simulation.

Trigger terms related to electrons, muons, and tracks were analyzed using reconstructed Z boson decays to dilepton final states. In each such decay, one lepton was matched to triggering and reconstruction requirements so that the other lepton could be used for unbiased efficiency measurements. This method, known as "*tag and probe*," was used to perform most of the high p_T lepton efficiency measurements used in the dilepton analyses. Hadronic jet triggers were studied using events passing either muon-based or electron-based triggers. Electron-triggered events were required to have exactly one electron that was both matched to electron trigger objects at all levels and separate from the jet considered in the efficiency measurement.

Efficiency measurements were parameterized in terms of the kinematic variables p_T, η, and ϕ of offline reconstructed objects. Uncertainties in these parameterizations were derived from fits to the observed variable distributions.

Separate efficiencies were estimated for Level 1 ($L1$), Level 2 ($L2$), and Level 3 ($L3$) conditions and the total event probability $P(L1, L2, L3)$ was estimated as

$$P(L1, L2, L3) = P(L1) \cdot P(L2|L1) \cdot P(L3|L1, L2), \quad (1)$$

where $P(L2|L1)$ and $P(L3|L1, L2)$ are the conditional probabilities for an event to satisfy a set of criteria provided it has already passed offline selection and previous levels of triggering. The overall trigger efficiency for $t\bar{t}$ events was then computed as the luminosity-weighted average of the event probabilities associated with each data taking period.

V. EVENT RECONSTRUCTION

A. Track Reconstruction

Charged particle trajectories were reconstructed from the patterns of energy deposits (or "hits") that they left in the tracking detectors. Track reconstruction at D0 involved two distinct steps: track finding and track fitting. Two complementary track finding algorithms were used in event reconstruction. The first is a histogramming approach based upon the Hough Transform — a method originally developed for finding tracks in bubble chambers [22]. An alternate track-finding approach began with groups of hits in the SMT barrels. These were fitted to a track hypothesis and the result was used to form a road in which to search for hits in additional detector layers.

The candidate track lists resulting from the two track-finding approaches were combined and passed to a Kalman [23] track fitter. This made use of an interacting propagator which propagates tracks through the D0 tracking system while taking into account magnetic curvature and interactions with detector material. The fitter incrementally adds hits to tracks using the input candidates to define roads. The resulting track fit allows for the calculation of optimal track parameters, with errors, on any surface.

The tracking momentum scale was determined by comparing the dimuon invariant mass distribution for $Z \to \mu\mu$ decays in data with expectation from simulation based upon the world average Z boson mass computed by the Particle Data Group [3]. In order for the simulated track momentum resolutions to match those observed in the data sample, an additional random smearing of track parameters was performed.

The measured transverse momentum resolution can be expressed as

$$\frac{\sigma(1/p_T)}{1/p_T} = \sqrt{\frac{(0.003 p_T)^2}{L^4} + \frac{(0.026)^2}{L \cdot \sin\theta}}. \quad (2)$$

Here p_T is measured in GeV and L is the *normalized track bending lever arm.* L is equal to 1 for tracks with $|\eta| < 1.62$ and is computed as $\tan\theta/\tan\theta'$ otherwise (θ' is the angle at which the track exits the tracker).

B. Primary Vertex Identification

The principal task of primary vertex (PV) finding is to identify tracks originating from the hard scatter and to separate these from tracks generated in superimposed minimum bias events. The algorithm first reconstructed one or more vertices and then selected the hard scatter vertex from among them by considering the p_T distribution and number of tracks associated with each vertex.

The vertex reconstruction algorithm included three steps: track clustering, track selection, and vertex fitting. First, tracks were clustered in z by considering their relative separations. Second, tracks kept for fitting were required to have at least 2 SMT hits and $p_T \geq 0.5$ GeV. Each track's distance of closest approach in the x-y plane (d_{CA}) to the nominal interaction position was also considered: the d_{CA} significance ($S = d_{CA}/\sigma_{d_{CA}}$) for a candidate track had to be less than 3. Finally, for every z cluster, an iterative vertex search yielded a vertex position. A probability that a vertex originated from a minimum-bias interaction was assigned based on the transverse momenta of its associated tracks. The vertex with the lowest probability was selected as the *primary*, or hard scatter, vertex. To further ensure the quality of selected primary vertex candidates, we required that they be within the SMT fiducial region ($|z_{PV}| \leq 60$ cm) and that they have at least three associated tracks.

In multijet data events, the position resolution of the primary vertex in the transverse plane is around 35 μm, convoluted with a typical beam spot size of 30 μm. The vertex resolution in the direction of the beam line is $\approx$1 mm.

C. Muon Identification

Muon identification was based on matches between charged particles found in the central tracking system and trajectories reconstructed in the muon systems. Tracks in the muon detectors comprised straight-line segments, or *stubs*, formed from combinations of scintillator and wire chamber hits in a single layer. Stubs were formed separately inside and outside the toroid iron and then paired together (provided their combinations were consistent with expectations for muons originating in the interaction region). Pairs were fitted to trajectories using knowledge of the toroidal magnetic field and the expected effects of energy loss and multiple scattering. The resulting *local* muon momenta were used, along with the directions of the muons at the inner surface of the muon system, to search for consistent central tracks with which to form a *global* match. Stubs that were not used in forming local muons were also used in global matches. In all cases, the results of the original central track fits were taken as the best estimates of muons' momenta, since the resolution of the central tracker is far superior to that of the local muon system.

To reduce the impact of muon detector noise, requirements were made on the number and location of scintillator and wire chamber hits. Two sets of muon quality requirements were used in the analyses discussed in this paper: *tight* and *loose*. Tight muons were required to have wire and scintillator hits both inside and outside the toroid iron. The loose criteria also accepted muons formed from single stubs with both types of hits either inside or outside the toroid.

Central tracks pointing into the fiducial volume of the muon detectors (*i.e.*, with $|\eta| < 2$) were considered as candidates for matches to muon tracks. To ensure that a central track was well-reconstructed, the χ^2 per degree of freedom of the Kalman fit used by the central tracking algorithm was required to be less than 4. Consistency between candidate tracks and the primary vertex was ensured by two additional cuts: the d_{CA} significance of each track must have been less than 3 and the smallest distance in z between it and the primary vertex (PV) must have been less than 1 cm. The quality criteria applied to central tracks and matching local muons are summarized in Table I.

Muons produced in top quark decays can be distinguished from those originating in heavy quark or other hadronic decays by a lack of nearby activity in the tracker and the calorimeter. This feature motivated two isolation criteria used to select signal candidate muons. These involved summing visible energies over a region around the central track associated with the muon. One variable was computed by summing the energies of reconstructed tracks and the other variable was derived from energy deposited in the calorimeter. For background muons, the size of either of these sums is correlated with the muon energy, while for signal it is not. Therefore, scaling the sums by the p_T of the candidate muon generates variables that tend to be higher for background than signal. A cut on either of these variables translates to an upper limit on surrounding visible energy that increases with muon p_T. Hence these variables provide more efficient criteria than the visible energy sums alone.

The track-based variable was computed as

$$\mathcal{E}^{\rm trk}_{\rm halo} = \frac{1}{p_T^{\mu}} \cdot \sum_{\Delta\mathcal{R}<0.5} p_T^{\rm trk}. \qquad (3)$$

Here $\Delta\mathcal{R}$ was defined for each muon-track pair as their separation in η-ϕ space, $\sqrt{\Delta\eta^2 + \Delta\phi^2}$. The track matched to the muon was excluded from the sum. Similarly, the calorimeter-based isolation was defined as

$$\mathcal{E}^{\rm cal}_{\rm halo} = \frac{1}{p_T^{\mu}} \cdot \sum_{0.1<\Delta\mathcal{R}<0.4} E_T^{\rm cell}, \qquad (4)$$

where the sum was over individual calorimeter cells. In each analysis channel that includes muons in its final state, signal candidate muons were required to have values of both $\mathcal{E}^{\rm trk}_{\rm halo}$ and $\mathcal{E}^{\rm cal}_{\rm halo}$ that are less than 0.12. This requirement was found to reject more than 99% of muons originating in hadronic jet decays and to be about 87% efficient for a muon coming from a top quark decay.

D. Electron Identification

High p_T electrons were identified by the presence of localized energy deposits in the electromagnetic calorimeter. Electron reconstruction began with the formation of clusters through the use of a simple cone algorithm that grouped calorimeter cells around seed cells having $E_T >$ 0.5 GeV. Any resulting cluster having $E_T > 1$ GeV was then grouped with all EM towers within a cone of radius $\Delta\mathcal{R} = 0.4$. The centroid of a cluster was calculated as the energy weighted mean value of the coordinates of its cells in the third layer of the EM calorimeter. Additional quality criteria were then applied to reject clusters resulting from photons and hadronic activity.

Electrons (and photons) deposit almost all of their energy in the EM section of the calorimeter while hadrons typically penetrate into the hadronic sections. Hence an electron is expected to have a large EM fraction (f_{EM}), which is defined as the ratio of summed energies deposited in the EM layers to the total energy deposited inside the clustering cone.

The longitudinal and lateral shower profiles of an EM cluster were required to be compatible with those of an electron (or photon). This was done by forming a $\chi^2_{\rm cal}$ based on a comparison of the energy depositions in each layer of the EM calorimeter and the total energy of the shower to average distributions obtained from Monte Carlo simulations.

Electrons produced in top quark decays can be distinguished from those originating in heavy quark or other hadronic decays by a lack of nearby activity in the

TABLE I: The quality criteria applied to muon candidates. Variable definitions are provided in the text.

Cut Level	Requirements
Loose	Local muon stubs inside and/or outside toriod iron, central track with $\chi^2_{\rm Kalman}/d.o.f. < 4$, $\sigma_{d_{CA}/d_{CA}} < 3$, and $\Delta z(\text{track}, \text{PV}) < 1$ cm
Tight	*Loose* and local muon stubs BOTH inside and outside toroid iron

calorimeter. The electromagnetic isolation fraction ($f_{\rm iso}$) was used to quantify the degree of isolation of an EM cluster and was defined as

$$f_{\rm iso} = \frac{E_{\rm tot}(\Delta\mathcal{R} < 0.4) - E_{EM}(\Delta\mathcal{R} < 0.2)}{E_{EM}(\Delta\mathcal{R} < 0.2)}, \quad (5)$$

where $E_{\rm tot}(\Delta\mathcal{R} < 0.4)$ is the total energy within a cone of size $\Delta\mathcal{R} = 0.4$ around the direction of the cluster, and $E_{EM}(\Delta\mathcal{R} < 0.2)$ is the energy in a cone of size $\Delta\mathcal{R} = 0.2$ summed over EM layers only.

In order to suppress photons and some hadronic jet backgrounds, an electron candidate was required to have an associated track in the central tracking system within $|\Delta\eta_{EM,\rm trk}| < 0.05$ and $|\Delta\phi_{EM,\rm trk}| < 0.05$ of the center of the EM cluster.

To further isolate real electrons, an *electron likelihood* formed from seven variables was computed. These variables included f_{EM}, $\chi^2_{\rm cal}$, the ratio of calorimeter transverse energy to track transverse momentum ($E_T^{\rm cal}/p_T^{\rm trk}$), the quality of the spatial matching between the central track and the EM cluster ($\chi^2_{{\rm spatial}EM-{\rm trk}}$), the d_{CA} of the track to the primary vertex, the number of tracks in a $\Delta R = 0.05$ cone, and the sum of the transverse momenta of all tracks in a cone of size $\Delta R = 0.4$ around the EM-associated track. Smoothed, normalized distributions of each of these variables were made from signal-like (*i.e.*, $Z \to ee$) events and background (*i.e.*, QCD dijet) data samples. For each discriminating variable x_i, these distributions provided probabilities $P^i_{\rm sig}(x_i)$ and $P^i_{\rm bkg}(x_i)$ for an EM object to be from a real and a fake electron, respectively. The following likelihood discriminant was used to distinguish between real electrons and fakes from hadronic objects.

$$\mathcal{L}_e(\mathbf{x}) = \frac{P_{\rm sig}(\mathbf{x})}{P_{\rm sig}(\mathbf{x}) + P_{\rm bkg}(\mathbf{x})}, \quad (6)$$

where $\mathbf{x}$ is the vector of likelihood variables. The probabilities were formed without regard to correlations between the likelihood variables, *i.e.*,

$$P_{\rm sig/bkg}(\mathbf{x}) = \prod_{i=1}^{7} P^i_{\rm sig/bkg}(x_i). \quad (7)$$

Three classes of electrons were considered on the basis of the aforementioned quantities: loose (or EM cluster), medium, and tight. The criteria applied to each category are listed in Table II. Less than 0.5% of all hadronic jets that passed loose EM object identification criteria survived the tight cuts. The efficiency of the medium quality cuts in data was found to be about 90% in the CC and about 63% in the EC. With respect to the medium requirements, the additional likelihood cut in the tight criteria is about 86% efficient in the CC and 84% efficient in the EC.

The ee analysis selected events with two tight electrons and the $e + track$ analysis used one tight electron. The $e\mu$ analysis had smaller backgrounds and therefore applied medium criteria to the signal electron candidate in each event. Because of the poor energy resolution for electrons reconstructed in the regions between the CC and EC sections, all electron-based analyses eliminated candidates having $1.1 < |\eta| < 1.5$. Electrons with $|\eta| > 2.5$ were also removed from consideration in order to suppress multiple scattering backgrounds.

The EM energy scale was established by requiring that the Z boson mass reconstructed in track-matched dielectron events match the world average Z boson mass computed by the Particle Data Group [3]. By requiring that both electrons in Z candidate events be in either the CC or the EC, independent absolute energy scale factors were obtained for each portion of the calorimeter. These were applied to high p_T electrons and photons. The calibration at lower energies was also checked using $J/\psi \to ee$ decays. The energy resolution for electrons in the CC or EC is $\sigma(E)/E \approx (15/\sqrt{E} \oplus 4)\%$ or $\sigma(E)/E \approx (21/\sqrt{E} \oplus 4)\%$, respectively (here E is measured in units of GeV).

E. Jet Identification

Particle jets were reconstructed from energy deposition in the calorimeter using a seed-based, improved legacy cone algorithm [24] with a cone radius of $\Delta\mathcal{R} = 0.5$. In this scheme, seeds were formed by clustering calorimeter cells above an energy threshold of 0.5 GeV. All resulting pre-clusters having summed energies above 1.0 GeV were then fed into an iterative clustering algorithm. If any of the resulting proto-jets shared energy, they were either split or merged so that each calorimeter tower was assigned to at most one reconstructed jet. Finally, only those jets having energies of at least 8 GeV were retained for further consideration.

Additional quality criteria were applied to clustered jets to suppress backgrounds originating from noise and other instrumental effects. Some of these selection cuts were based on variables that discriminate against particu-

TABLE II: The quality criteria applied to electron candidates. Variable definitions are provided in the text.

Cut Level	Requirements
Loose (EM cluster)	$p_T^{\text{cluster}} > 1.5$ GeV, $f_{EM} > 0.9$, $f_{\text{iso}} < 0.20$, and $\lvert\eta\rvert < 1.1$ OR $1.5 < \lvert\eta\rvert < 2.5$
Medium	*Loose* and $f_{\text{iso}} < 0.15$, $\chi^2_{\text{cal}} < 50$, and central track match
Tight	*Medium* and $\mathcal{L}_e > 0.85$

lar sources of noise. The *coarse hadronic fraction* (f_{CH}) is the fraction of the total energy in a jet that is contained in the outer, noisier layers of the calorimeter. The *hot fraction* (f_{hot}) is the ratio of the energy of the most energetic cell in a jet to that of its next-to-highest energy cell. Both f_{hot} and N_{90} (the number of cells containing 90% of the total energy in a jet) were used to suppress jets clustered around single cells that fired erroneously. Since noise generally did not appear simultaneously in the precision readout chain and in the separate Level 1 trigger readout, the ratio of the Level 1 energy to the precision readout energy in a jet ($f_{L1 \sum E_T}$) is another powerful discriminant against jets due to noise.

Other requirements were made on jet candidates to remove clusters that don't originate from partons generated in the hard scatter. The EM fraction (f_{EM}, see Sec. V D), was used to remove reconstructed electrons and photons. To eliminate backgrounds from low energy multiple interactions, far forward candidates were also eliminated. The particular values of all jet quality cuts are summarized in Table III.

After these initial cuts, some electrons still remained among the reconstructed jet objects. In order to avoid the resulting ambiguity, jet candidates overlapping medium quality electrons (see Table II) within $\Delta\mathcal{R} = 0.5$ were considered only as EM objects.

A data-to-Monte-Carlo correction factor that accounts for possible differences in the jet reconstruction and identification efficiencies was determined with back-to-back γ+jet events by requiring E_T balance between the photon and the jet. An E_T-dependent scale factor was then obtained separately for the CC, EC and ICD regions and applied to Monte Carlo.

A number of effects — including non-linearities in calorimeter response, non-instrumented material, and noise — can cause the measured jet energy to differ from the original particle-level energy. Jet energy scale (JES) corrections were applied to adjust jet energies to the particle level. Transverse momentum conservation in samples of γ + jet events was used to calibrate JES corrections in data and simulation. A more detailed description of this procedure is available in Ref. [25]. The relative uncertainty on the jet energy calibration is $\approx 7\%$ for jets with $20 < p_T < 250$ GeV.

Jet momentum resolutions were measured using dijet and γ+jet events. For 50 GeV jets in the CC or EC, the resolution was found to be $\sigma(p_T)/p_T \approx 13\%$ or $\sigma(p_T)/p_T \approx 12\%$, respectively.

F. Missing Transverse Energy

The presence of one or more neutrinos in an event is indicated by an imbalance of the visible momentum in the transverse plane. Calculation of this quantity began with the vector sum of the transverse energies of all calorimeter cells surviving various noise suppression algorithms, with the possible exception of cells in the coarse hadronic layers. These were included only if they are clustered within a reconstructed jet. The vector opposite to the result is called the *raw missing transverse energy* ($\not\!\!E_T^{\text{raw}}$).

As EM and jet energy scale corrections were applied to calorimeter objects, $\not\!\!E_T^{\text{raw}}$ was adjusted through vector subtraction. Only jets that pass the quality criteria listed in Table III were used for the hadronic part of this correction. The result is called the *calorimeter missing transverse energy* ($\not\!\!E_T^{\text{cal}}$).

Since muons are minimum ionizing particles, they deposit only a small fraction of their energy in the calorimeter and $\not\!\!E_T^{\text{cal}}$ does not properly account for their presence. Therefore, the momenta of all the identified muons of tight quality (see Table I) in an event were subtracted vectorially from $\not\!\!E_T^{\text{cal}}$ after first deducting the muons' expected energy depositions in the calorimeter. For the $\mu\mu$ analysis, isolated *loose* muons which did not pass tight quality requirements were also removed from $\not\!\!E_T^{\text{cal}}$. A similar procedure was followed for the track identified with a signal muon in the μ+track analysis. The fully corrected imbalance is simply called the *missing transverse energy* ($\not\!\!E_T$).

G. b Jet Tagging

Bottom quark jets were identified using a secondary vertex tagging (SVT) algorithm that exploits the long lifetime of b hadrons. The algorithm used is the same as that used in previously published D0 $t\bar{t}$ production cross section measurements [8, 9].

The SVT procedure began by clustering tracks in z into track jets. Track jets were reconstructed using a $\Delta\mathcal{R} = 0.5$ cone algorithm to cluster tracks with $p_T > 0.5$ GeV, at least two SMT hits, and $|d_{CA}| < 0.15$ cm. The z-projection of a candidate track's d_{CA} onto the beam line (z_{dca}) was required to be within 0.4 cm of the z position of the PV.

Within each track jet, tracks having d_{CA} significances greater than 3.5, χ^2/d.o.f. less than 3, and transverse momentum greater than 1 GeV were paired to form seed

TABLE III: The quality criteria applied to jet candidates. Variable definitions are provided in the text.

Cut	Target
$0.05 < f_{EM} < 0.95$	Noise and EM particles
$f_{CH} < 0.4$	Noise in coarse hadronic layers
$f_{\text{hot}} < 10$	Jets clustered around single cell
$N_{90} > 1$	Jets clustered around single cell
$f_{L1 \sum E_T} > 0.4$ ($\lvert\eta\rvert < 0.7$)	Noise in readout
$f_{L1 \sum E_T} > 0.2$ ($0.7 < \lvert\eta\rvert < 1.6$)	Noise in readout
$\lvert\eta\rvert < 2.5$	Extra soft scattering interactions in an event

vertices. Vertices consistent with having come from γ conversions or K^0_S or Λ decays were removed from consideration. Additional tracks pointing to a surviving seed were attached to it based on their contribution to the vertex χ^2. Vertices resulting from this process were selected as secondary vertex (SV) candidates based upon the collinearity of their component tracks, the χ^2 of their fits, and their decay length significances ($L_{xy}/\sigma_{L_{xy}}$). Here L_{xy}, the decay length, is the distance between the primary and secondary vertices in the plane transverse to the beam line and $\sigma_{L_{xy}}$ includes the uncertainty in the primary vertex position. The decay length can be positive or negative, depending on the sign of its projection onto the track jet axis. Secondary vertices corresponding to the decay of b and, to some extent, c hadrons are expected to have large positive decay lengths.

A calorimeter jet was tagged as a b jet if a secondary vertex with $L_{xy}/\sigma_{L_{xy}} > 7$ was found within $\Delta\mathcal{R} < 0.5$. If a jet contained at least one secondary vertex with $L_{xy}/\sigma_{L_{xy}} < -7$, the jet was labeled *negatively tagged*. Negative tags resulted from fake or mis-reconstructed tracks, or from the effects of multiple scattering in detector material. Negative tags were used to estimate the probability to misidentify a light flavor (a u, d, or s quark or a gluon) jet as a b jet (the *mis-tagging rate*).

The overall event tagging probability for a particular process depends upon the flavor composition of the jets in the final state and on the event kinematics. This probability was estimated through the application of tagging rates measured in data to each jet in simulation. A brief description of tagging probability measurements is given here, and a more detailed discussion is available in Ref. [9].

In order to decouple tagging efficiency measurements from detector geometry effects, jets considered for tagging were required to pass additional *taggability* criteria. A taggable jet had to have its axis matched to within $\Delta\mathcal{R} < 0.5$ with the axis of a track jet. The SMT hit requirement for tracks in track jets means that most taggable jets are associated with PV z positions within ≈36 cm of the center of D0 detector. Within this range, jets with momenta above 30 GeV typically have taggabilities of greater than 90%.

The b tagging efficiency was estimated using a sample of dijet events enriched in semileptonic decays of bottom and charm hadrons by the requirement that one jet have an associated muon. The heavy flavor content of this sample was further enriched by requiring that the opposite jet was tagged, either with the SVT algorithm or with a *soft lepton* tag. Soft lepton tagging requires that a muon with a momentum component along the direction orthogonal to the jet axis of at least 0.7 GeV be found within $\Delta\mathcal{R} = 0.5$. In order to extract the SVT tagging efficiency, both tagging algorithms were applied separately and together to the dijet sample. The resulting b tagging efficiency depends upon both η and p_T, and a typical 40 GeV taggable jet from top quark decay is tagged about 40% of the time. Charm quark jets have tagging efficiencies around 20% as large as those for b quarks. Light quark mis-tagging probabilities are on the order of 0.1%.

VI. ANALYSES

A. General Considerations

As discussed in Sec. I B, $t\bar{t}$ decays to dilepton final states are characterized by the presence of two high p_T charged leptons, significant $\not\!\!E_T$ from two neutrinos, and two or more jets (from b quark fragmentation and initial and final state radiation). Analysis of all four channels described here therefore begins by requiring that signatures consistent with two isolated, oppositely charged leptons and at least two jets be reconstructed.

The backgrounds at this stage vary with the channel considered, but generally include Drell-Yan production of (Z/γ^*)+jets, diboson production (*i.e.*, WW or WZ) with jets, and leptonic W+jets events in which another lepton arises from the misidentification of one of the jets. Resonant production of Z bosons which decay into electron or muon pairs is the dominant background for the ee and $\mu\mu$ channels, each of which employed cuts based upon $\not\!\!E_T$ and the invariant mass of the lepton pair to target this process.

The remaining backgrounds were removed using a combination of kinematic and topological constraints. These include a summed transverse energy H_T, defined as

$$H_T = p_T^{\ell_1} + \sum_{i=1}^{2} p_T^{j_i}; \tag{8}$$

where ℓ_1 denotes the highest p_T lepton, and i in the summation extends over the two highest p_T jets in the event.

For the $e\mu$ analysis, a cut on H_T was found to be more effective than one on $\not\!\!E_T$ in rejecting $Z \to \tau\tau$ background.

Analyses using fully reconstructed leptons (*i.e.*, the $e\mu$, ee, and $\mu\mu$ channels) were optimized separately to achieve the best possible performance using kinematic and topological quantities to supress dominant backgrounds. In order to recover some of the efficiency lost due to lepton identification requirements, an alternate approach using one fully reconstructed lepton and one central track was taken. To contend with the additional background let in by the lack of lepton identification requirements on the second lepton, the ℓ+track analysis required that at least one jet pass explicit b quark tagging requirements. The ee, $\mu\mu$, and ℓ+track selections are not completely orthogonal, and their overlaps were accounted for in the combined cross section calculation discussed in Sec. VII. The low-background $e\mu$ analysis was designed to have no overlap with the other channels.

B. The $e\mu$ Channel

The signature for an $e\mu$ event consists of one high p_T isolated electron, one high p_T isolated muon, and two or more jets. The major backgrounds to this channel come from Drell-Yan production of τ pairs which in turn decay to produce an $e\mu$ pair (*i.e.*, $Z/\gamma^* \to \tau\tau \to e\mu + X$) and WW production with jets. There are additional backgrounds present from misidentified leptons, particularly electrons. These are mostly $W(\to \mu\nu)$+3 jet events in which one of the jets was misidentified an electron. Hereafter, objects misidentified as electrons will also be referred to as *fake* electrons.

Offline selection began with medium electron and tight muon identification cuts (see Secs. V D and V C for details). To reject bremsstrahlung events, in which the muon emits a photon that is mistakenly identified as an electron, the candidate electron and muon were not allowed to share a common track in the central tracking detectors. Additionally, the candidate electron and muon were required to be matched to tracks of opposite charge.

After this initial lepton selection, the sample was dominated by background consisting of roughly equal amounts of misidentified leptons and physics processes leading to legitimate $e\mu$ pairs. The backgrounds generally contain jets arising from initial and final state radiation. These tend to be softer in p_T than the b jets that are generated in $t\bar{t}$ decays. Requiring that two or more jets (Sec. V E) be found with p_T of at least 20 GeV reduces both backgrounds by more than a factor of 50 while preserving more than two-thirds of the signal.

In addition to basic lepton and jet identification and energy requirements, the use of event-wide selection criteria was found to improve the expected significance of the result. Several variables were considered, including $\not\!\!E_T$, H_T, and the transverse mass of the combination of the leptons and the $\not\!\!E_T$. The performances of cuts on these quantities, whether alone or in combination, were evaluated using the expected significance of the background subtracted yield, including both the statistical uncertainties of the yields and a term reflecting the dominant jet energy scale systematic uncertainty in the total background estimate. It was found that requiring at least 122 GeV of H_T gave the best performance. Figure 1 shows the H_T distributions for signal and background before this cut and illustrates its ability to discriminate signal from background. Table IV shows the impact of the H_T cut on expected signal and background yields.

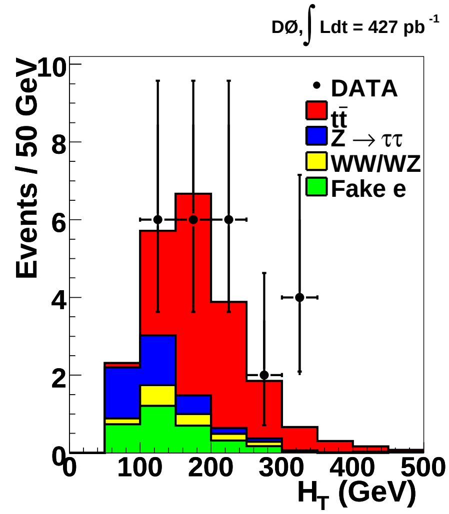

FIG. 1: H_T distributions in the $e\mu$ channel for expected signal (assuming $m_t = 175$ GeV and $\sigma_{t\bar{t}} = 7$ pb), expected background, and data after both lepton and jet requirements (corresponding to the second line of Table IV).

After all cuts are applied, 21 events remain in the data. Table V shows the expected background and signal (assuming $m_t = 175$ GeV and $\sigma_{t\bar{t}} = 7$ pb) contributions to the final sample.

Contributions from the processes $Z \to \tau\tau \to e\mu + X$ and $WW/WZ \to e\mu$+X were calculated using the Monte Carlo samples discussed in Sec. III. The background from fake electrons was estimated by performing an extended unbinned likelihood fit to the observed electron likelihood (Sec. V D) distribution in events passing all selection criteria. The distribution, which is shown in Fig. 2, was fitted using a likelihood given by

$$\mathcal{L} = \prod_{i=1}^{N} [n_e S(x_i) + n_{\mathrm{fake}} B(x_i)] \frac{e^{-(n_e + n_{\mathrm{fake}})}}{N!}, \qquad (9)$$

where i is an index that runs over all selected events, x_i is the corresponding observed value of the electron likelihood, N is the total number of events, n_e is the number of events with signal-like electrons, n_{fake} is the number of events having fake electrons, and S and B are the signal and background probability distribution functions, respectively. The event counts n_e and n_{fake} were allowed to float in the fit.

TABLE IV: Numbers of observed and expected $e\mu$ events passing the analysis cuts. The instrumental background is from fake electrons. Expected number of $t\bar{t}$ events are for $m_t = 175$ GeV and $\sigma_{t\bar{t}} = 7$ pb. Uncertainties correspond to statistical and systematic contributions added in quadrature.

	Data	Total sig+bkg	Instrumental bkg	Physics bkg	$t\bar{t}$
Trigger, 1 e, $p_T^e > 15$ GeV					
+ $\geq$1 μ, $p_T^\mu > 15$ GeV					
+ $\geq$2 jets, $p_T^{\rm jet} > 20$ GeV	24	$22.0^{+3.3}_{-2.9}$	$3.2^{+2.8}_{-2.0}$	$4.9^{+1.2}_{-1.4}$	$13.8^{+1.5}_{-1.7}$
+ $H_T > 122$ GeV	21	$17.7^{+2.9}_{-2.4}$	$2.1^{+2.5}_{-1.7}$	$2.5^{+0.7}_{-0.7}$	$13.1^{+1.4}_{-1.6}$

TABLE V: A more detailed listing of the expected $e\mu$ signal and background yields presented on the last line of Table IV. The expected number of $t\bar{t}$ events is calculated assuming $m_t = 175$ GeV and $\sigma_{t\bar{t}} = 7$ pb. Uncertainties include statistical and systematic contributions added in quadrature.

Process	Expected number of $e\mu + X$ events
$t\bar{t}$ (MC)	$13.09^{+1.42}_{-1.65}$
$Z \to \tau\tau \to e\mu + X$ (MC)	$1.46^{+0.38}_{-0.45}$
$WW/WZ \to e\mu + X$ (MC)	$0.99^{+0.40}_{-0.42}$
Fake leptons (data)	$2.14^{+2.50}_{-1.66}$
Total background	$4.58^{+2.56}_{-1.77}$

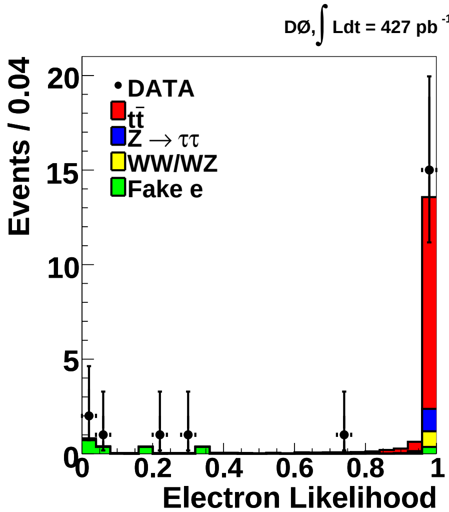

FIG. 2: The electron likelihood distribution in the $e\mu$ channel. Data passing all selection criteria are shown with points. The fake electron background estimated by a fit to the data points is shown, along with the simulated likelihood distributions for the each of the estimated signal and other background contributions, as shaded histograms.

The probability distribution functions used in the fit were determined with separate data samples enhanced in signal-like and background-like electrons. The signal probability distribution function came from a fit to the likelihood distribution of electrons in oppositely signed dielectron events selected using standard electron identification cuts and having low $\not\!\!E_T$. The background probability distribution function was determined using events passing all signal selection criteria but the jet requirements and using an anti-isolation cut on the muon. The contribution from signal-like electrons to the resulting sample was found to be less then 0.5%. Note that the fake electron estimate resulting from Eq. 9 includes backgrounds containing both real and fake isolated muons. The contribution from events containing legitimately identified electrons and falsely isolated muons was also investigated and found to be negligible.

C. The ee Channel

The signature for an ee event consists of two high p_T isolated electrons, at least two high p_T jets, and substantial $\not\!\!E_T$. The main background to this signature arises from Drell-Yan production of dielectrons ($Z/\gamma^* \to ee$). Although this process produces no real $\not\!\!E_T$, mismeasured $\not\!\!E_T$ can originate from misreconstructed jet or electron energies or from noise in the calorimeter. Other backgrounds include Drell-Yan production of τ pairs which further decay to dielectrons ($Z/\gamma^* \to \tau\tau \to ee + X$) as well as diboson ($WW/WZ$) production associated with jets. There are also small backgrounds from $W(\to e\nu)$+multijet and QCD multijet events in which one or two jets are misidentified as isolated electrons. The background from heavy flavor ($c\bar{c}$, $b\bar{b}$) production is negligible since electrons from these decays are typically soft and non-isolated.

Event selection began with two tight electrons, as described in Sec. V D, each having $p_T > 15$ GeV. The electrons were also required to have matching central tracks of opposite charge. This initial selection essentially eliminated any background from heavy flavor production and significantly reduced the background from misidentified electrons. The additional requirement that two jets be found, each with $p_T > 20$ GeV, generated a sample dominated by Drell-Yan Z/γ^* production with associated jets. Table VI shows the ee sample composition at this and subsequent stages of selection.

Simultaneous cuts on the $\not\!\!E_T$ and the dielectron invariant mass (M_{ee}) provide a powerful way to suppress most of the $Z/\gamma^* \to ee$ background. We vetoed events with M_{ee} values near the Z boson mass (*i.e.*, 80 GeV $< M_{ee} <$ 100 GeV) and required $\not\!\!E_T > 35$ GeV ($\not\!\!E_T > 40$ GeV) for

TABLE VI: Numbers of observed and expected ee events passing the analysis cuts. The instrumental background includes events containing misidentified electrons and misreconstructed $\not\!\!E_T$. Expected number of $t\bar{t}$ events are for $m_t = 175$ GeV and $\sigma_{t\bar{t}} = 7$ pb. Uncertainties correspond to statistical and systematic contributions added in quadrature.

	Data	Total sig+bkg	Instrumental bkg	Physics bkg	$t\bar{t}$
Trigger, $N_e \geq 2$, $p_T^e > 15$ GeV					
+ $\geq$2 jets, $p_T^{\rm jet} > 20$ GeV	369	$428.4^{+79.3}_{-77.1}$	$415.9^{+79.3}_{-77.1}$	$5.9^{+0.6}_{-1.4}$	$6.6^{+0.6}_{-0.6}$
+ M_{ee} cut	88	$106.2^{+19.0}_{-23.0}$	$98.6^{+19.0}_{-23.0}$	$1.9^{+0.3}_{-0.6}$	$5.7^{+0.5}_{-0.6}$
+ $\not\!\!E_T$ cut	5	$5.7^{+0.5}_{-0.6}$	0.7 ± 0.2	$0.7^{+0.2}_{-0.3}$	$4.3^{+0.4}_{-0.5}$
+ sphericity cut	5	$5.2^{+0.5}_{-0.5}$	0.5 ± 0.2	$0.6^{+0.2}_{-0.2}$	$4.0^{+0.4}_{-0.5}$

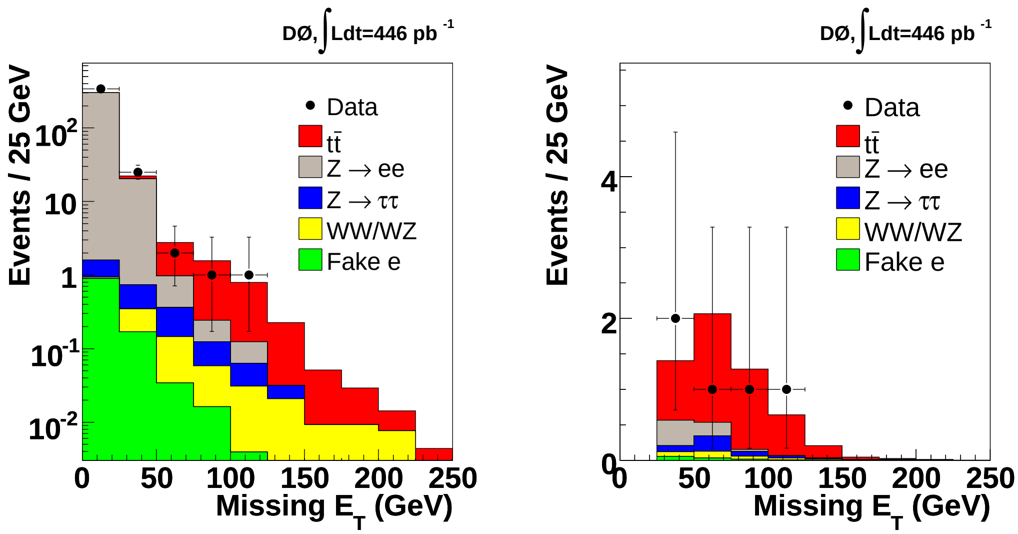

FIG. 3: Expected and observed $\not\!\!E_T$ distributions in dielectron events before (left) and after (right) cutting on M_{ee} and $\not\!\!E_T$.

$M_{ee} > 100$ GeV ($M_{ee} < 80$ GeV). These requirements effectively suppressed the $Z/\gamma^* \rightarrow ee$ background and brought other backgrounds to a manageable level while preserving significant signal efficiency. Their effect is illustrated in Fig. 3.

Finally, a cut on the sphericity of the event was applied in order to take advantage of the topological peculiarities of $t\bar{t}$ events and gain even more discrimination between signal and background. Sphericity ($\mathcal{S}$) is defined as

$$\mathcal{S} = \frac{3}{2}(\epsilon_1 + \epsilon_2), \quad (10)$$

where ϵ_1 and ϵ_2 are the two leading eigenvalues of the event-normalized momentum tensor [26]. The tensor ($\mathcal{M}_{xy}$) is calculated as

$$\mathcal{M}_{xy} = \frac{\sum_i p_x^i p_y^i}{\sum_i (p^i)^2}, \quad (11)$$

where the index i runs over the leading two electrons and the leading two jets in the event.

Sphericity can take values between 0 and 1. The applied cut of $\mathcal{S} > 0.15$ rejects events in which jets are produced in a planar geometry due to gluon radiation and provides a reasonable reduction in most of the backgrounds. The cut value was chosen using a figure of merit related to the expected statistical significance of the background subtracted signal. The observed and expected sphericity distributions for events passing the M_{ee} and $\not\!\!E_T$ cuts are shown in Fig. 4.

TABLE VII: A more detailed listing of the expected ee signal and background yields presented on the last line of Table VI. The expected number of $t\bar{t}$ events is calculated assuming $m_t = 175$ GeV and $\sigma_{t\bar{t}} = 7$ pb. Uncertainties include statistical and systematic contributions added in quadrature.

Process	Expected number of $ee + X$ events
$t\bar{t}$ (MC)	$4.04^{+0.40}_{-0.46}$
$Z \rightarrow \tau\tau \rightarrow ee + X$ (MC)	$0.35^{+0.11}_{-0.15}$
$WW/WZ \rightarrow ee + X$ (MC)	$0.23^{+0.11}_{-0.16}$
Mismeasured $\not\!\!E_T$ (data)	0.45 ± 0.15
Fake electron (data)	0.09 ± 0.03
Total background	$1.12^{+0.22}_{-0.27}$

After all cuts, five events remain in the data. Table VII shows the the expected background and signal (assuming $m_t = 175$ GeV and $\sigma_{t\bar{t}} = 7$ pb) contributions to the final sample.

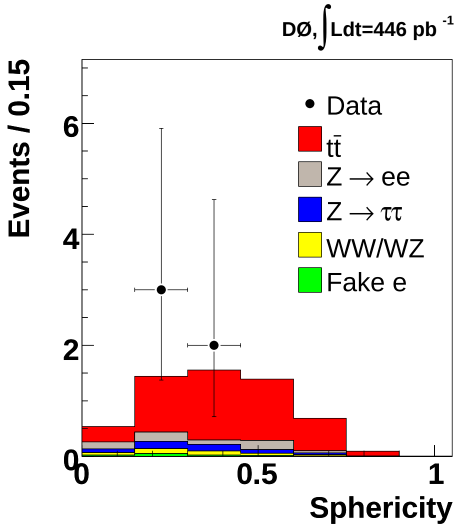

FIG. 4: The observed and predicted sphericity distributions of dielectron events after the M_{ee} and $\not\!\!E_T$ cuts.

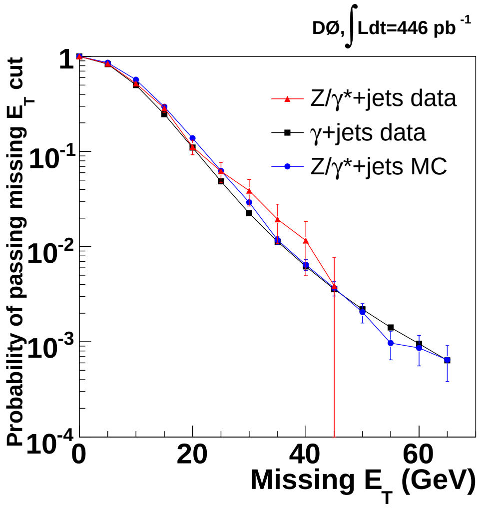

FIG. 5: The probability to pass the $\not\!\!E_T$ selection for events with two or more jets in $Z/\gamma^* \to e^+e^-$ data, in $\gamma + 2$ jets data, and for $Z/\gamma^* \to e^+e^-$ Monte Carlo.

The background contributions from $Z/\gamma^* \to \tau\tau$ and $WW/WZ(\to ee + X)$ decays were estimated using the Monte Carlo samples described in Sec. III. Simulated data were also used to estimate contributions from $Z/\gamma^* \to ee$ decays for cut levels prior to the $\not\!\!E_T$ requirement in Table VI. The background due to mismeasured $\not\!\!E_T$ was estimated from data using the observed *misreconstruction probability* ($f_{\rm MET}$) in γ+2 jets events selected to have kinematics and resolutions similar to the Z/γ^* backgrounds. Figure 5 shows that the $\not\!\!E_T$ spectrum in $Z/\gamma^* \to ee$ events with two or more jets is in good agreement with that observed in the γ+2 jets sample. We therefore estimated $f_{\rm MET}$ as the fraction of γ+2 jets events passing the $\not\!\!E_T$ selection.

The $\not\!\!E_T$ misreconstruction probability was multiplied by the number of events that failed the $\not\!\!E_T$ cut but passed all other selections. Thus the number of expected $\not\!\!E_T$ background events summed over the low and high M_{ee} regions is

$$N_{\rm MET}^{\rm misreco} = N_{M_{ee}<80{\rm GeV}} \times f_{\rm MET}^{40\ {\rm GeV}} + N_{M_{ee}>100{\rm GeV}} \times f_{\rm MET}^{35\ {\rm GeV}}. \tag{12}$$

The background due to electron misidentification was also obtained from data by calculating the fake electron probability, f_e. This was derived from a control sample containing two loose EM objects and passing signal dielectron triggers. Additional cuts on $\not\!\!E_T$ and M_{ee} were used to suppress contributions from signal-like electrons, and the resulting sample was found to be completely dominated by fake electrons.

The predicted number of fake electrons in the final sample ($N_e^{\rm fake}$) was obtained by multiplying the number of events with one loose and one tight electron by f_e. At this stage, $N_e^{\rm fake}$ contains both W+jet and QCD multijet backgrounds. The latter enters into the sample when two jets mimic the signal electron signature and misreconstructed $\not\!\!E_T$ allows the events to pass full selection criteria. Since this background was counted along with the misreconstructed $\not\!\!E_T$ background obtained from the data, it was removed from the $N_e^{\rm fake}$ estimate to avoid double counting. This was achieved by loosening identification cuts on both electron candidates in the final sample and scaling the yield by the square of f_e. This led to an estimate of N_{QCD} that was used to correct $N_e^{\rm fake}$.

D. The $\mu\mu$ Channel

The signature for a $\mu\mu$ event consists of two high p_T isolated muons, two high p_T jets, and large $\not\!\!E_T$. The dominant background in the dimuon channel comes from Drell-Yan production of muon pairs ($Z/\gamma^* \to \mu\mu$) in which misreconstructed objects give rise to mismeasured $\not\!\!E_T$. Other backgrounds include Drell-Yan production of τ pairs which decay to produce muon pairs ($Z/\gamma^* \to \tau\tau \to \mu\mu + X$) as well as WW and WZ production with jets. There are also backgrounds from multijet and W+jets events, in which one or more muons from heavy flavor decay pass isolation criteria. Hereafter, this class of muons will also be referred to as *fake* isolated muons.

Candidate events were required to contain two loose, isolated muons (as described in Sec. V C) with matching central tracks of opposite charge and two jets with $p_T > 20$ GeV. The first line of Table VIII shows signal and background yields after this initial event selection. The data selected are heavily dominated by misidentified Drell-Yan events. Two additional selection requirements were designed to specifically target this background. The first was a contour cut made in the plane formed by event $\not\!\!E_T$ and the opening angle in ϕ between the leading

TABLE VIII: Numbers of observed and expected $\mu\mu$ events passing the analysis cuts. The instrumental background includes events containing fake isolated muons and misreconstructed $\not\!\!E_T$. Expected number of $t\bar{t}$ events are for $m_t = 175$ GeV and $\sigma_{t\bar{t}} = 7$ pb. Uncertainties correspond to statistical and systematic contributions added in quadrature.

	Data	Total sig+bkg	Instrumental bkg	Physics bkg	$t\bar{t}$
Trigger, $N_\mu \geq 2$, $p_T^\mu > 15$ GeV					
$+ N_{\text{jets}} \geq 2 p_T^{\text{jet}} > 20$ GeV	387	$382.8^{+23.9}_{-23.5}$	$371.6^{+23.6}_{-23.2}$	$3.7^{+0.9}_{-0.9}$	$7.6^{+0.7}_{-0.7}$
$+ \Delta\phi(\mu_{\text{leading}}, \not\!\!E_T)$–$\not\!\!E_T$ cut	5	$6.2^{+0.8}_{-1.0}$	$1.7^{+0.3}_{-0.5}$	$0.5^{+0.2}_{-0.1}$	$4.0^{+0.4}_{-0.5}$
$+ \chi^2 > 4$	2	$3.6^{+0.5}_{-0.5}$	$0.3^{+0.1}_{-0.2}$	$0.4^{+0.1}_{-0.1}$	$3.0^{+0.3}_{-0.4}$

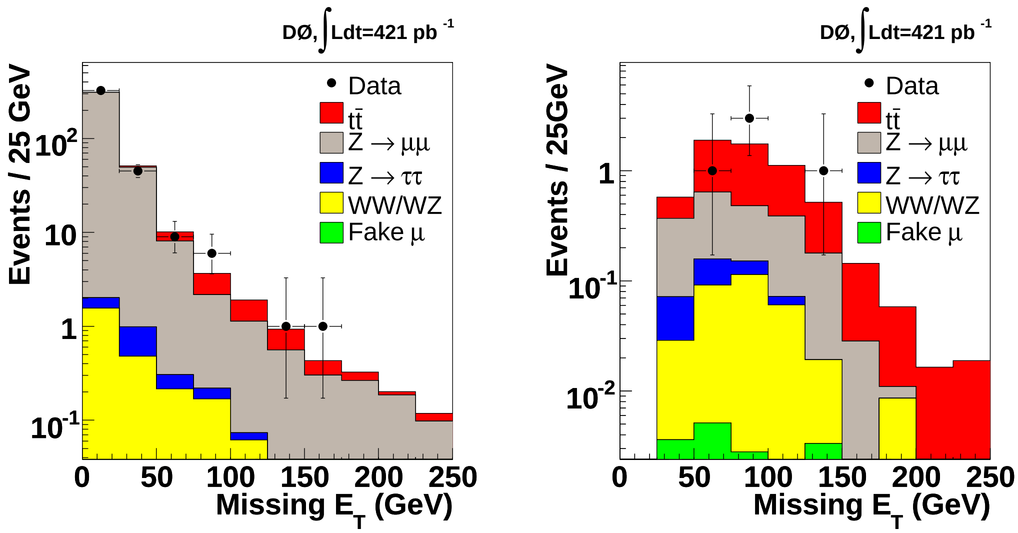

FIG. 6: Expected and observed $\not\!\!E_T$ distributions in dimuon events before (left) and after (right) the two-dimensional cut in the $\Delta\phi(\mu_{\text{leading}}, \not\!\!E_T)$ versus $\not\!\!E_T$ plane.

p_T muon and the $\not\!\!E_T$. Correlations between these two variables are caused by the misreconstruction of central tracks matched to muons. An event having $\not\!\!E_T$ less than 45 GeV was immediately rejected. This cut was further tightened at low and high values of $\Delta\phi(\mu_{\text{leading}}, \not\!\!E_T)$ to $\not\!\!E_T > 90$ GeV and $\not\!\!E_T > 95$ GeV respectively. Events with $\Delta\phi(\mu_{\text{leading}}, \not\!\!E_T) > 175°$ were removed. As can be seen in Fig. 6 and the second line of Table VIII, the contour cut effectively suppressed the misidentified background.

Further background rejection was achieved by cutting on the compatibility of an event with the $Z \to \mu\mu$ hypothesis. To this end, a χ^2 was formed using a Z boson mass constraint and the measured muon momentum resolution. The resulting variable, shown in Fig. 7, accounts for the p_T and η dependence of the tracking resolution and was found to perform better than a simple dimuon mass cut. The final cut value ($\chi^2 > 4$) and the location and shape of the contour cut described above were chosen using a grid search over Monte Carlo predictions of signal and background yields. Both cuts were varied simultaneously in the search and the best combination was chosen using a figure of merit related to the expected statistical significance of the background subtracted signal and including the expected uncertainty on the $Z + 2$ jets background prediction.

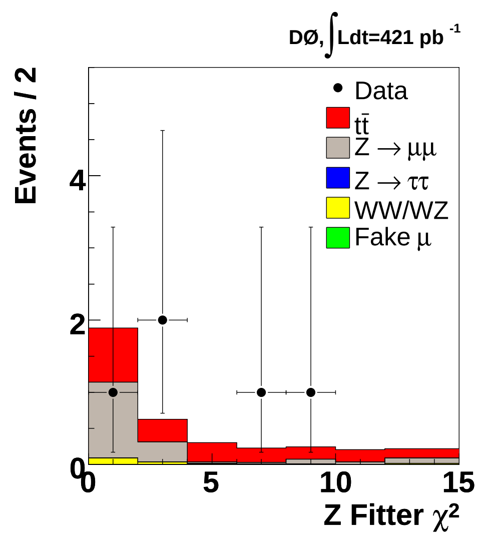

FIG. 7: The observed and predicted χ^2 distributions of dimuon events before the χ^2 cut.

After all cuts, two events remain in the data. Table IX shows the expected background and signal (as-

TABLE IX: A more detailed listing of the expected $\mu\mu$ signal and background yields presented on the last line of Table VIII. The expected number of $t\bar{t}$ events was calculated assuming $m_t = 175$ GeV and $\sigma_{t\bar{t}} = 7$ pb. Uncertainties include statistical and systematic contributions added in quadrature.

Process	Expected number of $\mu\mu + X$ events
$t\bar{t}$ (MC)	$2.96^{+0.31}_{-0.35}$
$WW/WZ \to \mu\mu + X$ (MC)	$0.19^{+0.10}_{-0.07}$
$Z \to \mu\mu/\tau\tau(\to \mu\mu)$+$X$ (MC)	$0.47^{+0.17}_{-0.18}$
Isolation fakes (data)	$0.01^{+0.01}_{-0.01}$
Total bkg	$0.67^{+0.24}_{-0.22}$

suming $m_t = 175$ GeV and $\sigma_{t\bar{t}} = 7$ pb) contributions to the final sample.

Background estimates for $Z \to \mu\mu$, $Z \to \tau\tau \to \mu\mu$+$X$, and WW/WZ production were calculated using the Monte Carlo samples discussed in Sec. III. The background from fake isolated muons was estimated using a procedure requiring two samples of events: a "tight" sample containing N_T events passing all the dimuon selection criteria and a "loose" sample of N_L events for which only one muon was required to pass isolation cuts. These event counts are related to the numbers of events with signal-like muons (N_{sl}) and events with background-like muons (N_{bl}) via the relations:

$$N_L = N_{sl} + N_{bl} \tag{13}$$

and

$$N_T = \epsilon_{\rm sig} N_{sl} + f_\mu N_{bl}. \tag{14}$$

Here $\epsilon_{\rm sig}$ is the probability for signal-like muons to pass isolation requirements and f_μ is the probability for muons in background events to pass isolation requirements. Equations 13 and 14 can be solved for the falsely isolated muon background in the fully selected sample (*i.e.*, $f_\mu N_{bl}$).

The faking probability was estimated as the isolation efficiency for the second highest p_T muon in dimuon events. To eliminate bias from W and Z boson decays, events in the sample were also required to have non-isolated leading muons and dimuon masses less than 70 GeV. The isolation efficiency for signal-like muons was estimated with ALPGEN $t\bar{t} \to \mu\mu + X$ Monte Carlo.

E. The ℓ+track Channel

The final state in the ℓ+track channel is characterized by two oppositely charged high p_T leptons, one explicitly reconstructed as an electron or a muon and the other identified as an isolated track. Requiring an isolated track as opposed to a fully reconstructed lepton allows the recovery of some events lost due to lepton reconstruction inefficiency and also adds a small number of events with a hadronically decaying tau lepton to the sample (5%/4% of the e+track/μ+track data). Events were also required to contain two high p_T jets and a large $\not\!\!E_T$. The dominant background in this channel originates from Drell-Yan production of lepton pairs ($Z/\gamma^* \to ee$ or $Z/\gamma^* \to \mu\mu$) where misreconstructed objects, resolution effects or noise can give rise to mismeasured $\not\!\!E_T$. Additional instrumental backgrounds arise from multijet and W+jets events, where a jet can be misidentified as an isolated lepton or track. Sources of irreducible (physics) backgrounds are $Z/\gamma^* \to \tau\tau$ and WW/WZ production in association with jets.

Selected events were required to have one tight, isolated lepton (electron or muon) with $p_T > 15$ GeV and an oppositely charged isolated track with $p_T > 15$ GeV. Neither the lepton nor the isolated track was allowed to be found within the cone of a reconstructed jet. In addition, the lepton and the isolated track were required to be separated in $\Delta\mathcal{R}$ by requiring $\Delta\mathcal{R}$(lepton, track) > 0.5.

A track was considered isolated if $\mathcal{E}^{\rm trk}_{\rm halo}$, defined in Eq. 3, was less than 0.12. The quality criteria applied to the isolated track were identical to those applied to the central muon tracks, with the exception of the d_{CA} significance requirement, where $\sigma_{d_{CA}}/d_{CA} < 5$ was used.

The candidate events were further required to have two or more jets, each with $p_T > 20$ GeV. The sample selected by the above requirements is dominated by Z/γ^* background events. This background was partly removed by requirements on the $\not\!\!E_T$ in each event. For the μ+track channel, $\not\!\!E_T > 35$ GeV (> 25 GeV) was required for 70 GeV$\leq M_{\mu,\rm trk} \leq 110$ GeV ($M_{\mu,\rm trk} < 70$ GeV or $M_{\mu,\rm trk} > 110$ GeV). The corresponding cuts in the e+track channel were $\not\!\!E_T > 20$ GeV (> 15 GeV) for 70 GeV $\leq M_{e,\rm trk} \leq 100$ GeV ($M_{e,\rm trk} < 70$ GeV or $M_{e,\rm trk} > 100$ GeV). The tighter requirements for the μ+track channel reflect the impact of the muon-matched central track p_T resolution on the reconstructed transverse energy.

While the preceding requirements are effective, the most powerful discriminant used to suppress backgrounds in this analysis is the requirement of at least one b tagged jet, since jets in background events originate predominantly from light (u, d, or s) quarks or gluons. The b tagging algorithm and its performance are discussed in Sec. V G. Figure 8 shows the numbers of observed and predicted events with two or more jets as a function of H_T (defined in Eq. 8) before and after the secondary vertex requirement. The impact of the tagging requirement on the backgrounds is clearly visible. Tables X and XI show the impact of the $\not\!\!E_T$ and b tagging requirements on the expected signal and background yields.

After application of all selection criteria, 17 events remain in the data. Tables XII and XIII show the expected signal and background contributions to the final sample.

The b quark and c quark tagging efficiencies and mistag rate are parameterized as functions of jet p_T and $|\eta|$ (see Sec. V G). The tagging probabilities for $t\bar{t}$ events were estimated by applying these parameterizations to jets in simulated events.

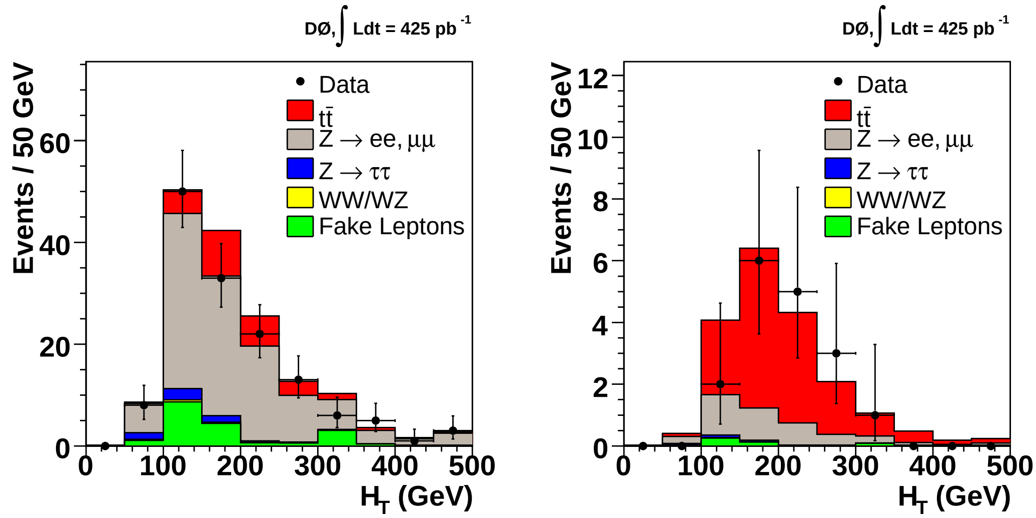

FIG. 8: H_T spectra of observed and predicted events in the ℓ+track channel before (left) and after (right) the secondary vertex requirement.

TABLE X: Numbers of observed and expected e+track events passing the analysis cuts. The instrumental background includes events containing misidentified electrons and misreconstructed $\not\!\!E_T$. Expected numbers of $t\bar{t}$ events are for $m_t = 175$ GeV and $\sigma_{t\bar{t}} = 7$ pb. Uncertainties correspond to statistical and systematic contributions added in quadrature.

	Data	Total sig+bkg	Instrumental bkg	Physics bkg	$t\bar{t}$
Trigger, e+track, $p_T^{e/trk} > 15$ GeV					
+ $\geq$2 jets, $p_T^{\rm jet} > 20$ GeV	436	$442.2^{+79.9}_{-72.1}$	$422.6^{+79.5}_{-71.3}$	$4.7^{+0.9}_{-1.1}$	$15.0^{+1.0}_{-0.9}$
+ $\not\!\!E_T$ cut	85	$92.2^{+20.8}_{-13.8}$	$74.5^{+20.5}_{-13.2}$	$3.8^{+0.7}_{-0.9}$	$13.8^{+1.0}_{-0.9}$
+ $\geq$ 1 b tagged jet	11	$10.9^{+1.2}_{-1.0}$	$2.7^{+0.9}_{-0.7}$	$0.1^{+0.0}_{-0.0}$	$8.1^{+0.7}_{-0.6}$

The $Z/\gamma^* \to ee/\mu\mu$, $Z/\gamma^* \to \tau\tau$, and diboson backgrounds were estimated using the simulated samples discussed in Sec. III. The b tagging probability for $Z/\gamma^* \to ee/\mu\mu$ events was estimated using a control sample selected with all ℓ+track event selection criteria with the exception of the $\not\!\!E_T$ cut, which was reversed. As a cross check, separate b tagging probabilities were measured for the e+track and μ+track channels and were found to be consistent. The b tagging efficiency for $Z/\gamma^* \to \tau\tau$ was taken to be the same as for $Z/\gamma^* \to ee, \mu\mu$ events. For diboson events, the b tagging efficiency was assumed to be the same as for W boson events with associated jet production.

The contribution from W boson and multijet events containing fake isolated leptons and/or tracks was estimated using specially selected data samples. The method employed is similar to that described for similar backgrounds in the dimuon analysis (Sec. VI D). Because the effects of loosening isolation requirements on leptons and tracks were included separately, the system of equations 13 and 14 expands to include four equations. The unknowns in each expression include the number of events with fake isolated tracks and fake isolated leptons (N^{ft}_{fl}), the event count with fake isolated tracks and real isolated leptons (N^{ft}_{rl}), the number of events with real isolated tracks and fake isolated leptons (N^{rt}_{fl}), and the event count with real isolated tracks and real isolated leptons (N^{rt}_{rl}). Once these quantities are obtained, backgrounds due to fake isolated leptons and/or tracks can be computed as

$$N_{W+\rm jets} = N^{ft}_{rl} + N^{rt}_{fl} \qquad (15)$$

and

$$N_{\rm QCD} = N^{ft}_{fl}. \qquad (16)$$

In order to limit the impact of statistical fluctuations, this procedure was applied to events selected without b tagging. The final background estimates were then derived using separate tagging efficiencies for W+jets and multijet backgrounds.

Knowledge of the efficiencies of the tight track and lepton criteria relative to their loose counterparts for both signal-like and background-like objects is required to extract the unknown yields from observed event counts. The efficiency for a signal-like loose electron, muon or track to pass each corresponding tight criterion was determined from simulated samples of $Z/\gamma^* \to ee$ and $\mu\mu$ events. The efficiencies for loose fake leptons were measured in a multijet data sample obtained by selecting

TABLE XI: Numbers of observed and expected μ+track events passing the analysis cuts. The instrumental background includes events containing fake isolated muons and misreconstructed $\not\!\!E_T$. Expected numbers of $t\bar{t}$ events are for $m_t = 175$ GeV and $\sigma_{t\bar{t}} = 7$ pb. Uncertainties correspond to statistical and systematic contributions added in quadrature.

	Data	Total sig+bkg	Instrumental bkg	Physics bkg	$t\bar{t}$
Trigger, μ+track, $p_T^{\mu/trk} > 15$ GeV					
+ ≥2 jets, $p_T^{\rm jet} > 20$ GeV	480	$483.5^{+89.4}_{-82.8}$	$465.8^{+88.7}_{-82.0}$	$4.5^{+0.9}_{-1.1}$	$13.1^{+1.0}_{-1.0}$
+ $\not\!\!E_T$ cut	56	$63.8^{+10.1}_{-10.1}$	$50.4^{+9.6}_{-9.5}$	$2.6^{+0.7}_{-0.9}$	$10.8^{+0.9}_{-0.9}$
+ ≥ 1 b tagged jet	6	$8.3^{+0.8}_{-0.8}$	$1.9^{+0.6}_{-0.6}$	$0.1^{+0.0}_{-0.0}$	$6.3^{+0.6}_{-0.6}$

TABLE XII: A more detailed listing of the expected e+track signal and background yields presented on the last line of Table X. The expected number of $t\bar{t}$ events is calculated assuming $m_t = 175$ GeV and $\sigma_{t\bar{t}} = 7$ pb. Uncertainties include statistical and systematic contributions added in quadrature.

Process	Expected number of e+track events
$t\bar{t}$ (MC)	$8.08^{+0.08}_{-0.08}$
WW (MC)	$0.02^{+1.09}_{-1.09}$
$Z \to ee, \mu\mu$ (MC)	$2.29^{+0.40}_{-0.31}$
$Z \to \tau\tau$ (MC)	$0.12^{+0.31}_{-0.35}$
W/multijet (data)	$0.42^{+0.37}_{-0.37}$
Total bkg	$2.85^{+0.33}_{-0.27}$

TABLE XIII: A more detailed listing of the expected μ+track signal and background yields presented on the last line of Table XI. The expected number of $t\bar{t}$ events is calculated assuming $m_t = 175$ GeV and $\sigma_{t\bar{t}} = 7$ pb. Uncertainties include statistical and systematic contributions added in quadrature.

Process	Expected number of μ+track events
$t\bar{t}$ (MC)	$6.29^{+0.09}_{-0.09}$
WW (MC)	$0.01^{+1.10}_{-1.12}$
$Z \to ee, \mu\mu$ (MC)	$1.83^{+0.31}_{-0.30}$
$Z \to \tau\tau$ (MC)	$0.08^{+0.36}_{-0.46}$
W/multijet (data)	$0.08^{+0.88}_{-0.88}$
Total bkg	$2.00^{+0.29}_{-0.30}$

lepton events in a low $\not\!\!E_T$ (<10 GeV) region. Biases from Z boson decays were removed by eliminating events with two like-flavor leptons or with an additional isolated track that, when paired with the lepton, formed an invariant mass consistent with M_Z. Efficiencies for loose fake tracks were measured in similarly chosen samples.

Secondary vertex tagging efficiencies for W+jets events were measured using single-lepton events selected with the same Z boson rejection criteria used for the multijet sample described above. Additional biases from the presence of top quark pairs were accounted for by subtracting predicted $t\bar{t}$ contributions calculated with an assumed production cross section of 7 pb. The event tagging probabilities for multijet events were determined using the same multijet data samples used to estimate isolation faking probabilities.

TABLE XIV: Numbers of observed events, expected background yields, the product of $t\bar{t}$ selection efficiency times branching ratio, and the integrated luminosity for each analysis channel. The branching fractions for the $e\mu$, ee and $\mu\mu$ channels considers the decays $t\bar{t} \to b\bar{b}WW \to e\mu/ee/\mu\mu + X$ respectively. Both e+track and μ+track channels consider $t\bar{t} \to b\bar{b}WW \to \ell\ell + X$ decays ($\ell = e, \mu, \tau$) with the τ leptons decaying both leptonically and hadronically.

Channel	$N_{\rm obs}$	$N_{\rm bkg}$	$\epsilon \times \mathcal{B}$ (%)	$\int \mathcal{L}dt$ (pb^{-1})
$e\mu$	21	$4.58^{+2.56}_{-1.77}$	0.44 ± 0.04	427 ± 26
ee	5	$1.12^{+0.22}_{-0.27}$	0.13 ± 0.02	446 ± 27
$\mu\mu$	2	$0.67^{+0.24}_{-0.22}$	0.10 ± 0.02	421 ± 26
e+track	11	$2.85^{+0.33}_{-0.27}$	0.27 ± 0.02	425 ± 26
μ+track	6	$2.00^{+0.29}_{-0.30}$	0.21 ± 0.02	422 ± 26

F. Summary

Table XIV presents a summary of event counts observed in data, expected background yields, the products of $t\bar{t}$ selection efficiencies and branching ratios, and luminosities for each of the five dilepton analysis channels. These quantities enter into the top quark pair production cross section calculations discussed in Secs. VII A and VII C.

VII. CROSS SECTION CALCULATION

A. Individual Channel Cross Sections

To estimate the production cross section σ_j for an individual dilepton channel j, the following likelihood function was defined:

$$L(\sigma_j, \{N_j^{\rm obs}, N_j^{\rm bkg}, \varepsilon_j \times \mathcal{B}_j, \mathcal{L}_j\}) = \mathcal{P}(N_j^{\rm obs}, n_j) = \frac{n_j^{N_j^{\rm obs}}}{N_j^{\rm obs}!}\, e^{-n_j}, \quad (17)$$

where $\mathcal{P}(N_j^{\rm obs}, n_j)$ is the Poisson probability to observe $N_j^{\rm obs}$ events given an expected combined signal and background yield of

$$n_j = \sigma_j\,(\varepsilon_j \times \mathcal{B}_j)\,\mathcal{L}_j + N_j^{\rm bkg}. \quad (18)$$

TABLE XV: The $t\bar{t}$ production cross sections at $\sqrt{s}$ = 1.96 TeV and for a top quark mass of 175 GeV as measured in each analysis channel. The first uncertainty listed for each result is statistical in origin. The second uncertainty is the combined effect of all systematics, excluding the uncertainty on the luminosity measurement. The final error listed is from the luminosity measurement. The origins of the systematic uncertainties are discussed in Sec. VII B.

Channel	$\sigma_{t\bar{t}}$ (pb)
$e\mu$	$8.8\ ^{+2.6}_{-2.3}\ ^{+1.4}_{-1.1}\ \pm0.5$
ee	$6.7\ ^{+4.5}_{-3.3}\ ^{+1.1}_{-0.8}\ \pm0.4$
$\mu\mu$	$3.1\ ^{+4.2}_{-2.6}\ ^{+0.9}_{-0.9}\ \pm0.2$
e+track	$7.1\ ^{+3.2}_{-2.6}\ ^{+1.0}_{-1.2}\ \pm0.4$
μ+track	$4.5\ ^{+3.1}_{-2.4}\ ^{+0.9}_{-0.9}\ \pm0.3$

Here $\mathcal{L}_j$ is the luminosity, $\epsilon_j \times \mathcal{B}_j$ is the product of selection efficiency and branching fraction, and $N_j^{\rm bkg}$ is the expected background for channel j (see Table XIV). The cross section is then extracted by minimizing the negative log-likelihood function,

$$-\log L(\sigma_j, \{N_j^{\rm obs}, N_j^{\rm bkg}, \varepsilon_j \times \mathcal{B}_j, \mathcal{L}_j\}). \qquad (19)$$

The results are presented in Table XV.

B. Systematic Uncertainties

Systematic uncertainties for the analyses can be broadly grouped into those related to signal acceptance calculations and those concerning overall background estimates. Brief descriptions of the sources of systematics are provided below.

- *Primary vertex identification*
A correction to the simulated efficiency for primary vertex selection was estimated by comparing its value in $Z \to ee/\mu\mu$ decays in data and Monte Carlo. In order to quote a systematic uncertainty related to this correction, the ratio of data and Monte Carlo efficiencies was varied by $\pm1\sigma$, and signal efficiencies and expected background yields were re-computed. The ultimate origin of the uncertainty σ is the statistical limitations of the $Z \to ee/\mu\mu$ data samples.

- *Lepton identification*
For electrons and muons, uncertainties related to the identification and selection criteria described in Secs. V C and V D were estimated using control samples of $Z \to ee/\mu\mu$ decays. The tag and probe technique discussed in Sec. IV was used to compute the effects of each criterion in data and Monte Carlo, and the ratio of the resulting efficiencies was used to correct the simulation. When a correction was found to depend on object kinematics, it was binned appropriately. The corresponding systematic uncertainty was computed by varying the correction by $\pm1\sigma$, where σ arose from the statistical limitations of the Z boson control samples in data.

- *Track reconstruction*
Analyses using muons and the ℓ+track channels include uncertainties associated with central track reconstruction. Chief among these is the uncertainty in the track smearing procedure discussed in Sec. V A. Signal efficiency and background yield calculations were repeated with the smearing parameters varied according to their uncertainties, whose ultimate origin is in the parameterization of the smearing functions and the size of the data samples used to tune them. Because of the significance of Bremsstrahlung energy loss for electrons, separate uncertainties were used for the e+track channel.

- *Jet identification*
This uncertainty corresponds to the correction to simulated jet identification and quality requirement efficiencies described in Sec. V E.

- *Jet energy calibration*
This uncertainty includes contributions estimated for the jet energy scale and resolution corrections described in Sec. V E.

- *Trigger simulation*
Uncertainties on the fits to the trigger efficiencies for each object discussed in Sec. IV were propagated to estimate event triggering systematics.

- *Background estimation*
For background estimates using Monte Carlo simulations, normalization uncertainties were calculated using theoretical and/or experimental uncertainties in the corresponding product of production cross section and decay branching ratios. For instance, a systematic uncertainty of 35% is associated to the normalization of diboson+jets background, taken very conservatively as the difference between LO and NLO cross sections. For backgrounds estimated from data, systematic uncertainties have their ultimate origin in the statistical limitations of the relevant control samples.

- *$t\bar{t}$ tagging probability*
For the ℓ+track channels, additional uncertainties associated with the b quark tagging probability in $t\bar{t}$ decays (Sec. V G) were included. The dominant sources of uncertainty arise from the method used to extract the b tagging efficiency in data and from the limited statistics in the heavy flavor enriched data samples.

- *Background tagging probability*
For the ℓ+track channels, uncertainties in the

b tagging probabilities for the background processes (Sec. VI E) were also taken into account. These originated from limited statistics in the background-enriched data samples and observed dependence of the event tagging probability on $\not\!\!E_T$. For the W+jets events, where the $t\bar{t}$ contamination was subtracted assuming a cross section of 7 pb, the effect of varying the $t\bar{t}$ cross section between 5 and 9 pb was propagated to the final result.

- *Luminosity*
  The integrated luminosity corresponding to each of the data samples used by the analyses has a fractional uncertainty of 6.1% [12].

- *Other uncertainties*
  Statistical uncertainties related to the sizes of Monte Carlo and data samples used independently for each channel are uncorrelated between them. These and other less important uncertainties are combined in this category.

For each channel, an uncertainty on the cross section was obtained for each independent source of systematic uncertainty by varying the source by $\pm 1\sigma$ and propagating the variation into both background estimates and the signal efficiency. A new likelihood function was derived for each such variation to give a new optimal cross section. The resulting variations in the central value of the cross section are presented in Table XVI.

C. Combined Cross Section

Calculation of the combined estimate of the $t\bar{t}$ production cross section using all of the results presented in Table XV is complicated by the fact that some of the selection criteria are correlated. Specifically, the ee criteria are correlated with those of the e+track analysis, and the $\mu\mu$ and μ+track criteria overlap. To account for this, we apply a BLUE technique (*i.e.*, Best Linear Unbiased Estimate) [27].

The correlations between the top quark pair selection efficiencies of the non-orthogonal analysis pairs were estimated with psuedo-experiments drawn from Monte Carlo samples. The ee–e+track and $\mu\mu$–μ+track correlations were found to be 43% and 47%, respectively. The use of b tagging in the ℓ+track selections resulted in negligible correlations between the backgrounds surviving each channel's selection.

Correlations between the systematic uncertainties of each of the analyses were also included in the combination. These were taken as 100%, −100%, or 0%, as appropriate. Furthermore, all asymmetric uncertainties were made symmetric by averaging their positive and negative values. The combined cross section was derived using an iterative process. The combination in each iteration step was performed using the expected statistical and systematic uncertainties evaluated at the cross section obtained

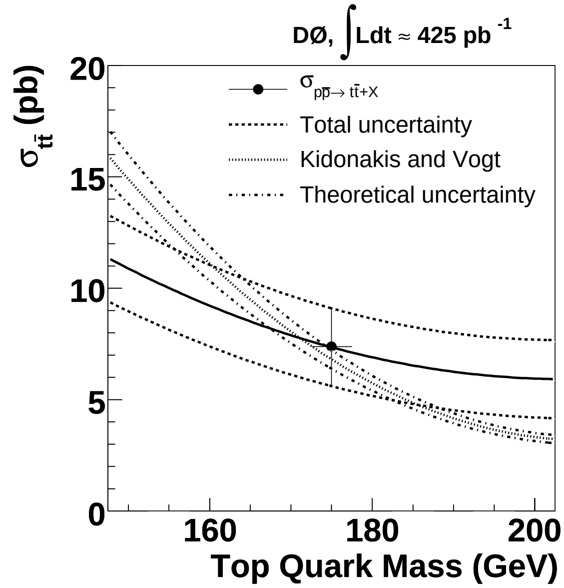

FIG. 9: The dependence of the measured cross section on the top quark mass compared to the theoretical prediction [4, 5].

in the previous iteration step. The use of expected uncertainties avoids over-weighting the results of downward fluctuations. It was verified that the result of the iterative process was independent of the cross section input to the first iteration. The calculation was repeated until the result was stable to within 0.01% between iterations. The resulting combined cross section is

$$\sigma_{t\bar{t}} = 7.4 \pm 1.4\,(\mathrm{stat}) \pm 0.9\,(\mathrm{syst}) \pm 0.5\,(\mathrm{lumi})\,\mathrm{pb} \quad (20)$$

for a top quark mass of 175 GeV. There were a total of four degrees of freedom in the combination, and the χ^2 of the result is 1.6. Table XVII lists the relative weight of each analysis channel's result in the combination. The $e\mu$ measurement dominates the result, with the two ℓ+track results entering with the next most significant weights. Table XVIII presents the contribution of each individual systematic uncertainty described in Sec. VII B to the total error on the result.

The dependence of the result on the top quark mass was computed using parameterizations of each channel's selection efficiency as a function of m_t. For a set of assumed masses, the individual channel results and their combination were recalculated using the appropriate efficiency. The result is shown in Fig. 9. For values of m_t between 170 GeV and 180 GeV, the value of the measured cross section as a function of top quark mass is approximated by:

$$\sigma_{t\bar{t}}(m_t) = 7.4\,\mathrm{pb} - 0.1\frac{\mathrm{pb}}{\mathrm{GeV}} \times (m_t - 175\,\mathrm{GeV}). \quad (21)$$

For the current Tevatron average of top quark mass of 170.9 GeV [28], the resulting value of the cross section is 7.8 ±1.8 (stat+syst) pb.

TABLE XVI: A summary of the effects of individual systematic uncertainties on each channel's measured cross section. Quantities are presented in percent change from the central values presented in Table XV.

Source	$e\mu$		ee		$\mu\mu$		e+track		μ+track	
PV identification	0.5	−0.5	0.5	−0.5	0.7	−0.5	0.6	−0.6	0.7	−0.7
Lepton identification	6.3	−5.9	9.1	−8.2	3.8	−3.5	4.3	−4.2	7.8	−7.2
Track reconstruction	4.2	−4.6	0.1	−0.1	8.8	−10.3	3.4	−3.3	4.5	−4.0
Jet identification	4.8	−3.5	8.0	−4.0	13.2	−8.6	2.8	−6.3	6.6	−0.8
Jet energy calibration	7.1	−6.1	8.2	−5.4	22.0	−21.7	8.5	−11.2	10.0	−11.4
Trigger	10.2	−5.7	7.5	−1.9	5.5	−4.0	2.9	−2.3	5.5	−4.4
Bkg estimation	4.7	−3.7	2.1	−2.2	5.6	−5.4	2.5	−2.5	3.8	−3.9
$t\bar{t}$ tagging	0.0	−0.0	0.0	−0.0	0.0	−0.0	4.0	−3.8	4.0	−3.8
Bkg tagging	0.0	−0.0	0.0	−0.0	0.0	−0.0	7.0	−7.0	11.2	−11.2
Other	2.4	−2.3	2.3	−2.2	2.6	−2.4	2.2	−2.3	2.6	−2.7
Total	16.2	−12.5	16.7	−11.2	28.6	−26.7	13.9	−16.5	20.5	−19.6

TABLE XVII: Relative weight of each measurement in the combined cross section calculation.

Channel	Weight (%)
$e\mu$	53
e+track	22
μ+track	17
ee	4
$\mu\mu$	4
All	100

TABLE XVIII: A summary of the effects of individual systematic uncertainties on the combined cross section measurement.

Source	Uncertainty (pb)
PV identification	0.07
Lepton identification	0.41
Track reconstruction	0.09
Jet identification	0.30
Jet energy calibration	0.60
Trigger	0.39
Bkg estimation	0.22
$t\bar{t}$ tagging	0.11
Bkg tagging	0.19
Other	0.10
Total	0.94

VIII. CONCLUSION

We have measured the $t\bar{t}$ production cross section in $p\bar{p}$ collisions at $\sqrt{s} = 1.96$ TeV utilizing dilepton signatures in approximately 425 pb^{-1} of data collected with the D0 detector. The result, for $m_t = 175$ GeV, is

$$\sigma_{t\bar{t}} = 7.4 \pm 1.4\,(\text{stat}) \pm 1.0\,(\text{syst})\,\text{pb}. \qquad (22)$$

This is in good agreement with the theoretical prediction of $6.7^{+0.7}_{-0.9}$ pb from the full NLO matrix elements and the re-summation of the leading and next-to-leading soft logarithms [4, 5]. For the current Tevatron average of m_t = 170.9 GeV, the corresponding value of the measured cross section is 7.8 ±1.8 (stat+syst) pb.

IX. ACKNOWLEDGEMENTS

We thank the staffs at Fermilab and collaborating institutions, and acknowledge support from the DOE and NSF (USA); CEA and CNRS/IN2P3 (France); FASI, Rosatom and RFBR (Russia); CAPES, CNPq, FAPERJ, FAPESP and FUNDUNESP (Brazil); DAE and DST (India); Colciencias (Colombia); CONACyT (Mexico); KRF and KOSEF (Korea); CONICET and UBACyT (Argentina); FOM (The Netherlands); Science and Technology Facilities Council (United Kingdom); MSMT and GACR (Czech Republic); CRC Program, CFI, NSERC and WestGrid Project (Canada); BMBF and DFG (Germany); SFI (Ireland); The Swedish Research Council (Sweden); CAS and CNSF (China); Alexander von Humboldt Foundation; and the Marie Curie Program.

APPENDIX A: TRIGGER REQUIREMENTS

Tables XIX–XXIII list the trigger conditions used for each analysis channel. A description of the triggering system and details regarding particle reconstruction in each trigger subsystem are available in Sec. IV. As beam conditions changed and delivered instantaneous luminosity increased, trigger conditions were changed to maintain event selection rates within operational limits. The tables group triggers used together at the same time and present the total luminosity exposed to each grouping.

[*] Visitor from Augustana College, Sioux Falls, SD, USA.
[¶] Visitor from The University of Liverpool, Liverpool, UK.
[§] Visitor from ICN-UNAM, Mexico City, Mexico.
[‡] Visitor from Helsinki Institute of Physics, Helsinki, Finland.
[#] Visitor from Universität Zürich, Zürich, Switzerland.

TABLE XIX: Trigger requirements used to collect data for the $e\mu$ analysis. Total integrated luminosity exposed to each trigger set is given in the last column.

Level 1 conditions	Level 2 conditions	Level 3 conditions	Integrated luminosity (pb^{-1})
1 e, $E_T > 5$ GeV and 1 loose μ	none	1 loose e, $E_T > 10$ GeV	130.2
1 e, $E_T > 6$ GeV and 1 loose μ	none	1 loose e, $E_T > 12$ GeV	243.8
1 e, $E_T > 6$ GeV and 1 loose μ	1 μ	1 loose e, $E_T > 12$ GeV OR 1 tight e, $E_T > 7$ GeV OR 1 tight, track-matched e, $E_T > 5$ GeV	53.2

TABLE XX: Trigger requirements used to collect data for the ee analysis. Total integrated luminosity exposed to each trigger set is given in the last column.

Level 1 conditions	Level 2 conditions	Level 3 conditions	Integrated luminosity (pb^{-1})
2 e, $E_T > 10$ GeV	none	1 loose e, $E_T > 10$ GeV	23.3
2 e, $E_T > 10$ GeV	none	1 loose e, $E_T > 20$ GeV	120.2
1 e, $E_T > 11$ GeV OR 2 e, $E_T > 6$ GeV OR 2 e, $E_T^1 > 9$ GeV, $E_T^2 > 3$ GeV	none	2 loose e, $E_T > 20$ GeV OR 1 loose and 1 tight e, $E_T > 15$ GeV	252.2
1 e, $E_T > 11$ GeV OR 2 e, $E_T > 6$ GeV OR 2 e, $E_T^1 > 9$ GeV, $E_T^2 > 3$ GeV	2 e, $\sum E_T > 18$ GeV	2 loose e, $E_T > 20$ GeV OR 2 tight e, $E_T > 8$ GeV [a] OR 1 loose and 1 tight e, $E_T > 15$ GeV	49.8

[a]For part of the data, a 10 GeV E_T requirement was used.

[1] F. Abe *et al.* [CDF Collaboration], Phys. Rev. Lett. **74**, 2626 (1995).
[2] S. Abachi *et al.* [D0 Collaboration], Phys. Rev. Lett. **74**, 2632 (1995).
[3] W. M. Yao *et al.* [Particle Data Group], J. Phys. G **33**, 1 (2006).
[4] M. Cacciari, S. Frixione, M. L. Mangano, P. Nason, and G. Ridolfi, JHEP **0404**, 068 (2004).
[5] N. Kidonakis and R. Vogt, Phys. Rev. D **68**, 114014 (2003).
[6] C. T. Hill and S. J. Parke, Phys. Rev. D **49**, 4454 (1994).
[7] D. Acosta *et al.* [CDF Collaboration], Phys. Rev. Lett. **93**, 142001 (2004); A. Abulencia *et al.* [CDF Collaboration], Phys. Rev. Lett. **97**, 082004 (2006).
[8] V. M. Abazov *et al.* [D0 Collaboration], Phys. Lett. B **626**, 35 (2005).
[9] V. M. Abazov *et al.* [D0 Collaboration], Phys. Rev. D **74**, 112004 (2006).
[10] S. Abachi *et al.* [D0 Collaboration], Nucl. Instrum. Meth. A **338**, 185 (1994).
[11] V. M. Abazov *et al.* [D0 Collaboration], Nucl. Instrum. Meth. A **565**, 463 (2006).
[12] T. Andeen *et al.*, FERMILAB-TM-2365.
[13] M. L. Mangano *et al.*, JHEP **0307**, 001 (2003).
[14] H. L. Lai *et al.*, Eur. Phys. J. **C12**, 375 (2000).
[15] T. Sjöstrand *et al.*, Comp. Phys. Commun. **135** 238 (2001).
[16] D. J. Lange, Nucl. Instrum. Meth. A **462**, 152 (2001).
[17] S. Jadach *et al.*, Comp. Phys. Commun. **76**, 361 (1993).
[18] R. Brun and F. Carminati, CERN Program Library Long Writeup W5013, 1993 (unpublished).
[19] H. L. Lai *et al.*, Phys. Rev. D **55**, 1280 (1997).
[20] J. M. Campbell and R. K. Ellis, Phys. Rev. D **60**, 113006 (1999).
[21] G. C. Blazey *et al.*, arXiv:hep-ex/0005012.
[22] P. V. C. Hough, International Conference on High Energy Accelerators and Instrumentation, CERN (1959).
[23] R. E. Kalman, J. Bas. Eng. **82D**, 35 (1960); R. E. Kalman and R. S. Bucy, J. Bas. Eng. **83D**, 95 (1961).
[24] U. Baur (ed.), R. K. Ellis (ed.), and D. Zeppenfeld (ed.), FERMILAB-PUB-00-297 (2000).
[25] V. Abazov *et al.* [D0 Collaboration], FERMILAB-PUB-06-426-E (2006), submitted to Phys. Rev. D, arXiv:hep-ex/0612040v1.
[26] V. D. Barger, J. Ohnemus, and R. J. N. Phillips, Phys. Rev. D **48**, 3953 (1993).
[27] L. Lyons and D. Gibaut, Nucl. Instrum. Meth. A **270**, 110 (1988).
[28] The Tevatron Electroweak Working Group for the CDF and D0 Collaborations, arXiv:hep-ex/0703034v1.
[29] Note that these muon quality criteria differ from those discussed in Sec. V C.

TABLE XXI: Trigger requirements used to collect data for the $\mu\mu$ analysis. Each triggering regime has both a single muon and a dimuon requirement, each of which ties together trigger conditions at all three levels. Total integrated luminosity exposed to each trigger set is given in the last column.

Multiplicity	Level 1 conditions	Level 2 conditions	Level 3 conditions	Integrated luminosity (pb^{-1})
1	1 tight μ	1 μ, $p_T > 3$ GeV	1 track, $p_T > 10$ GeV	59.5
2	2 loose μ	1 μ	none	
1	1 tight μ	1 μ, $p_T > 3$ GeV	1 track, $p_T > 10$ GeV	66.5
2	2 loose μ	1 μ	1 μ, p_T >15 GeV OR 1 track, $p_T > 10$ GeV	
1	1 tight μ	1 μ, $p_T > 3$ GeV	1 track, $p_T > 10$ GeV	243.8
2	2 loose μ	1 μ	1 μ, $p_T > 6$ GeV OR 1 track, $p_T > 5$ GeV	
1	1 tight μ and 1 track, $p_T > 10$ GeV	1 μ, $p_T > 3$ GeV	1 μ, $p_T > 15$ GeV	51.5
2	2 loose μ	1 μ	1 μ, $p_T > 6$ GeV OR 1 track, $p_T > 5$ GeV	

TABLE XXII: Trigger requirements used to collect data for the e+track analysis. For some periods of data collection, a logical OR of multiple requirements was used. Each requirement tied together trigger conditions at all three levels. Total integrated luminosity exposed to each trigger set is given in the last column.

Level 1 conditions	Level 2 conditions	Level 3 conditions	Integrated luminosity (pb^{-1})
1 e, $E_T > 10$ GeV AND 2 jets, $E_T > 5$ GeV	1 e, $E_T > 10$ GeV AND 2 jets, $E_T > 10$ GeV	1 tight e, $E_T > 15$ GeV AND 2 jets, $E_T > 15$ GeV	127.8
1 e, $E_T > 11$ GeV	none	1 tight e, $E_T > 15$ GeV AND 2 jets, $E_T > 20$ GeV	244.0
1 e, $E_T > 11$ GeV OR 2 e, $E_T > 6$ GeV OR 2 e, $E_T > 3$ GeV, 1 e, $E_T > 9$ GeV	none	1 tight e, $E_T > 20$ GeV	
1 e, $E_T > 11$ GeV OR 2 e, $E_T > 6$ GeV OR 2 e, $E_T > 3$ GeV, 1 e, $E_T > 9$ GeV	none	1 loose e, $E_T > 50$ GeV	
1 e, $E_T > 11$ GeV	1 e, $E_T > 15$ GeV	1 tight e, $E_T > 15$ GeV AND 2 jets, $E_T > 20$ GeV AND 1 jet, $E_T > 25$ GeV	53.7
1 e, $E_T > 11$ GeV OR 2 e, $E_T > 6$ GeV OR 2 e, $E_T > 3$ GeV, 1 e, $E_T > 9$ GeV	1 e, $E_T > 15$ GeV	1 tight e, $E_T > 20$ GeV	
1 e, $E_T > 11$ GeV OR 2 e, $E_T > 6$ GeV OR 2 e, $E_T > 3$ GeV, 1 e, $E_T > 9$ GeV	1 e, $E_T > 15$ GeV	1 loose e, $E_T > 50$ GeV	

TABLE XXIII: Trigger requirements used to collect data for the μ+track analysis. For some periods of data collection, a logical OR of multiple requirements was used. Each requirement tied together trigger conditions at all three levels. Total integrated luminosity exposed to each trigger set is given in the last column.

Level 1 conditions	Level 2 conditions	Level 3 conditions	Integrated luminosity (pb^{-1})
1 loose μ AND 1 jet $E_T > 5$ GeV	1 μ	1 jet, $E_T > 20$ GeV	131.5
1 loose μ AND 1 jet, $E_T > 3$ GeV	1 μ AND 1 jet, $E_T > 10$ GeV	1 jet, $E_T > 25$ GeV	244.0
1 tight μ	1 μ, $p_T > 3$ GeV	1 track, $p_T > 10$ GeV	
1 tight μ AND 1 jet, $E_T > 5$ GeV	1 μ AND 1 jet, $E_T > 8$ GeV	1 jet, $E_T > 25$ GeV	30.3
1 loose μ w. trackmatch AND 1 track, $p_T > 10$ GeV	none	1 track, $p_T > 10$ GeV OR 1 μ, $p_T > 15$ GeV	
1 tight μ AND 1 track, $p_T > 10$ GeV	1 μ, $p_T > 3$ GeV	1 μ, $p_T > 15$ GeV	
1 loose μ AND 1 track, $p_T > 10$ GeV	1 μ	1 μ, $p_T > 15$ GeV	
1 tight μ AND 1 jet, $E_T > 5$ GeV	1 μ AND 1 jet, $E_T > 8$ GeV	1 μ, $p_T > 3$ GeV AND 1 jet, $E_T > 25$ GeV	16.0
1 loose μ w. trackmatch AND 1 track, $p_T > 10$ GeV	none	1 track, $p_T > 10$ GeV OR 1 μ, $p_T > 15$ GeV	
1 tight μ AND 1 track, $p_T > 10$ GeV	1 μ, $p_T > 3$ GeV	1 μ, $p_T > 15$ GeV	
1 loose μ AND 1 track, $p_T > 10$ GeV	1 μ	1 μ, $p_T > 15$ GeV	